Archives of Civil and Mechanical Engineering (2022) 22:140
https://doi.org/10.1007/s43452-022-00468-8

ORIGINAL ARTICLE

Study on effect of weld groove geometry on mechanical behavior and residual stresses variation in dissimilar welds of P92/SS304L steel for USC boilers

Gaurav Dak[1] · **Chandan Pandey**[1]

Received: 11 March 2022 / Revised: 19 April 2022 / Accepted: 16 May 2022 / Published online: 8 June 2022

Abstract
This research article reports the correlation between microstructure, mechanical properties, and residual stresses of dissimilar weld joints (DWJs) between P92 martensitic steel and 304L austenitic stainless steel (ASS). The groove geometry plays a vital role in DWJs. Thus the effect of groove geometry on mechanical and microstructural properties was also investigated. The V-shape and narrow shape groove profile were implemented for P92/304L SS DWJs. The microstructural characteristic, tensile strength, micro-hardness, Charpy impact toughness and residual stresses were evaluated for both the groove geometry in as-weld (AW) and post-weld heat treatment (PWHT) (760 °C, 2 h) state. Microstructural observations performed using an optical microscope (OM), and scanning electron microscope (SEM) showed that high temperature during the weld thermal cycle leads to the formation of the coarse grain heat-affected zone (CGHAZ), fine grain HAZ (FGHAZ), and inter-critical HAZ (ICHAZ) across the P92 HAZ. The ERNiFeCr-2 (Inconel 718) welding consumable wire (filler rod) of diameter 2.4 mm was used for this investigation. The ERNiFeCr-2 weld fusion zone showed a fully austenitic microstructure with the formation of the secondary phases due to the solidification segregation. The EDS and SEM area mapping results indicated that the secondary phases in the inter-dendritic region contain a higher amount of the Mo and Nb than the matrix region. The ultimate tensile strength (UTS) of the as-weld and PWHT tensile specimen of the P92/304L SS DWJs was 630 and 621 MPa, respectively, for V-groove geometry specimens and 620 and 629 MPa, respectively, for narrow groove geometry specimens. The tensile fracture was experienced at the interface between weld metal and 304L base metal, and the UTS value of DWJs was very close to the UTS of the 304L SS. The abrupt variation in the micro-hardness value of the CGHAZ (456HV0.5), FGHAZ (375HV0.5), and ICHAZ (221HV0.5) was noticed in the as-weld state due to their distinguish microstructure characteristics. After PWHT, the micro-hardness value of the CGHAZ (255HV0.5), FGHAZ (236HV0.5), and ICHAZ (207HV0.5) was below the maximum allowable value of 265HV0.5 for P92 material because of the tempering of the martensite. The Charpy impact test indicated that the ERNiFeCr-2 weld fusion zone has a low toughness value of 33 J (AW) and 25 J (PWHT) for V-groove design and 35 J (AW) and 28 J (PWHT) for narrow groove design than that of the P92 and 304L parent metal. The impact toughness of the ERNiFeCr-2 filler weld was below the minimum requirement of 47 J (EN ISO 3580:2017). The tensile residual stresses were generated in the weld fusion zone due to the volumetric contraction during the solidification. The residual stresses developed in the case of the narrow groove design were less than that for the V-groove design due to the less quantity of weld metal available for volumetric contraction in the case of the narrow groove geometry. From comparing mechanical and microstructural properties obtained for V-groove and narrow groove geometry DWJs, it was found that narrow groove design reduces the overall heat affected zone span, and it requires less welding time and less heat input.

Keywords P92 martensitic steel · 304L austenitic steel · ERNiFeCr-2 (Inconel 718) filler · Residual stress · Mechanical properties · Microstructure

✉ Chandan Pandey
jscpandey@iitj.ac.in; chandanpy.1989@gmail.com

Extended author information available on the last page of the article

1 Introduction

The critical components of the power plants are pipes, headers, superheater/reheater tubes, and water–wall tubes. The candidate materials for such components are ferritic-martensitic (F-M) steel, austenitic stainless steels (ASSs), and nickel-based super-alloy. The components such as pipes and headers are thick section components subjected to thermal fatigue during the cyclic operation. The essential properties requirements for such components are high-temperature creep strength, good thermal conductivity, low coefficient of thermal expansion, and excellent corrosion resistance [1]. Thus ferritic/martensitic steels are preferred for these components. However, they are suitable for temperatures only up to 620 °C [2]. The superheater/reheater tubes operate under high temperature and corrosive medium. The ASSs are used for the construction of superheaters and reheaters. The pipe linking the superheater and reheater is made of P92 steel [3]. Thus, to satisfy the design requirement and minimize the overall cost of the power plant, dissimilar weld joints (DWJs) between ferritic/martensitic steel and austenitic stainless steel become essential. The P92 steel is supposed to be a candidate material for the piping and tubes in ultra-supercritical (USC) and advanced ultra-supercritical (AUSC) power plants due to its good creep strength, high thermal conductivity, and low coefficient of thermal expansion (CTE) [4]. The ASSs such as 304L, 304H, and 316L are also commonly used in power plants due to their excellent corrosion resistance and low cost. The DWJs reduce the components' overall cost due to the saving on the expensive materials used in dissimilar joining. The DWJs are also used to meet the design flexibility of the components [5]. The DWJs between F-M steel and ASS are also used in pressurized water reactors (PWRs) in nuclear power plants to join the ferritic steel pipe-nozzles of the pressure vessels to the austenitic stainless steel safe-end pipes [6]. There can be over thousands of DWJs in a single thermal power plant. The application of the DWJs is not limited only to the power plants, but it is also frequently used in chemical, petrochemical, and offshore industries.

The successful DWJs can be obtained by selecting the appropriate filler metal. The nickel-based filler is most commonly used to achieve defect-free dissimilar joint of F-M steel and ASS (F-M/A) due to their superior mechanical and microstructural properties in severe conditions compared to the others [7, 8]. In the past years, austenitic filler metal was used to join ferritic and austenitic dissimilar metals. However, the DWJs prepared with austenitic filler result in the premature failure of the components under service due to the carbon migration and formation of the sigma phases [9]. Also, due to the carbon diffusion from ferritic steel towards the austenitic stainless steel, the formation of soft carbon-depleted zone (also called white bands) occurs at the ferritic/austenitic weld interface [10]. This deteriorates the creep strength of the weld joints [11]. The nickel-based filler also provides a longer service life of the components than the austenitic filler. It has been reported that nickel-based filler increases the service life of the F-M/A DWJs to five times compared to the austenitic filler [12]. Dupont et al. [13] reported that the increase in the service life of the F-M/A DWJs is because of the reduction in the thickness of the martensitic layer formed by the nickel-based filler compared to the austenitic filler. The ERNiFeCr-2 (Inconel 718) is precipitation strengthened nickel-based alloy with excellent strength and corrosion resistance at high temperatures. The Inconel 718 super-alloy gets its strengthening effect from γ''-Ni_3Nb precipitates [14]. It has been reported that Nb rich filler results in the Nb segregation in the weld fusion zone during the solidification. This forms the low melting point liquid film (NbC and Nb-rich Laves phase) in the inter-dendritic region, making it more prone to hot-cracking [15]. The Nb is the element that segregates most during solidification due to its partition coefficient (k) value of less than 1 ($k < 1$). The fully austenitic microstructure of the nickel-based filler results in the formation of the migrated grain boundaries (MGBs) in the weld metal. Some researchers reported that ductility dip cracking always occurs from the MGBs [16]. Devendranath et al. [17] performed the laser welding of the Inconel 718 and AISI 416. The authors reported the segregation of the Nb-rich laves phase at the weld fusion zone and liquation cracking at the HAZ of Inconel 718.

The application of P92 steel with 304L SS in power plants implies the joining of dissimilar metals. When this different combination of metal is fusion welded, problems such as the formation of delta ferrite, soft zone, unmixed zone, and type IV cracking susceptible ICHAZ region arise [18]. Thus, it becomes difficult to obtain the sound quality of the weld joint. For this reason, the joining of these two metals with nickel-based filler is generally carried out. Also, to improve the mechanical and microstructural properties after welding, PWHT is carried out. Tungsten inert gas (TIG) welding is a well-known technique for joining the various grades of steel due to its good weld quality and ability to produce defect-free and excellent strength weld joints. However, the limited penetration ability (~6 mm) of this welding process necessitates the use of filler metal and multi-pass weld [19, 20]. The high heat input to increase the weld penetration can lead to the deterioration of the mechanical properties. The properties such as creep strength, corrosion resistance, and high-temperature strength of the material mainly depend upon the material's microstructure. The high heat generated

during the welding deteriorates the microstructure of the material. Thus, to achieve the desirable weld property of the dissimilar joint, PWHT becomes essential [21]. Also, from the various literature reviewed, it was found that groove geometry also plays a vital role in DWJs. The narrow groove design results in less welding time and less weld metal deposition due to the low included angle. Also, a narrow groove design minimizes the weld distortion and residual stresses due to less heat input [22, 23]. However, the reduced gap between the plates to be joined in a narrow groove design makes it difficult for the welder to access the weld fusion zone properly. Thus, an expert welder is required for the welding with the narrow groove design. The defects such as lack of fusion may frequently occur during the narrow groove welding if proper attention is not given [24]. Nivas et al. [25] performed the TIG welding to join 20 mm-thick Low alloy steel and 304 LN austenitic stainless steel with a conventional V-groove and narrow gap groove profile. They observed the low HAZ width and better mechanical and microstructural properties for narrow gap profile due to less heat input. Giri et al. [26] investigated the effect of conventional and narrow groove geometry on the residual stress distribution for 25 mm-thick SS 304LN pipes. They observed a 10–15% reduction in the residual stress magnitude with the narrow groove design.

From several literatures reviewed, it was found that various researchers have reported the number of failures of such DWJs. Most of the failures were before the estimated service life of the DWJs because of the formation of the sigma phases, lave phases, coarsening of the precipitates, high stresses at the interface, carbon migration, and low oxidation resistance of ferritic steel at high temperature [12]. Thus, a systematic study is required to identify the performance of these dissimilar welds in actual service conditions. The detailed literature on the dissimilar joining of P92 steel and 304L SS using Inconel 718 filler is still not available in the public domain. This research work aims to investigate the effect of Inconel 718 filler on mechanical, microstructural, and residual stress properties of the martensitic and austenitic dissimilar weld in as-weld and PWHT states. The various investigations carried out after the welding and PWHT process are discussed in the subsequent sections.

2 Experimental

The base metal (BM) used in this study was 10 mm-thick plates of P92 steel and AISI 304L stainless steel. The P92 steel was used in normalized (1040 °C for 40 min and air-cooled) and tempered conditions (760 °C for 2 h and air-cooled), whereas the AISI 304L SS in the solution annealed was used for DWJs. The alloy composition of the base materials is listed in Tables 1 and 2, respectively. The microstructure of the P92 base materials is depicted in Fig. 1a–c. The normalizing heat treatment provides the lath martensite microstructure, and tempering heat treatment causes the evolution of the precipitates ($M_{23}C_6$ and MX), which are required for the creep and high-temperature strength. The P92 steel microstructure contains prior austenite grains (PAGs), lath packets, carbide ($M_{23}C_6$, M: Cr, Fe), and carbonitride (MX, M: V, Nb, X: C, N) precipitates as depicted in Fig. 1a, b. The $M_{23}C_6$ precipitates are generally bigger than MX precipitates, as depicted in Fig. 1c. The $M_{23}C_6$ precipitates are decorated along prior austenite grain boundaries (PAGBs), while MX precipitates are present in matrix and packet boundaries. The austenitic steel microstructure primarily consists of austenite grain and twins, as depicted in Fig. 1d, e. The rectangular plates with dimensions $150 \times 55 \times 10$ mm^3 were prepared from each base metal for the DWJs. Afterward, with the help of a shaper machine, a single v-groove and narrow groove butt joint configuration with a 37.5° groove angle was prepared at the edges of the plates to be joined. The root gap and root height were 1.5 mm each, respectively. The V-shape and narrow groove geometry prepared on P92 and 304L SS plates is shown in Fig. 2a–d. The dissimilar welding was performed using a

Table 1 Alloy composition (%wt.) of the P92 steel and 304L ASS

Material	C	Mn	P	S	Si	Cr	Ni	Others
P92 steel	0.093	0.41	0.019	0.004	0.21	8.60	0.31	W:1.98, Mo:0.45, V:0.18, Nb:0.052, N_2:0.060, Ni:0.31, Ti:0.001, Al:0.001, B:0.002, Zr:0.002, Fe: Rem
AISI 304L SS	0.018	1.12	0.024	0.011	0.42	18.05	8.06	Fe: Rem

Table 2 Alloy composition (%wt.) of the ERNiFeCr-2 filler metal

Material	C	Mn	P	Si	S	Cr	Mo	Cu	Fe	Nb	Al	Ni	Ti	Others
ERNiFeCr-2	0.05	0.03	0.002	0.0.06	0.0007	17.39	2.93	0.02	20.10	5.2	0.4	52.70	0.99	0.011

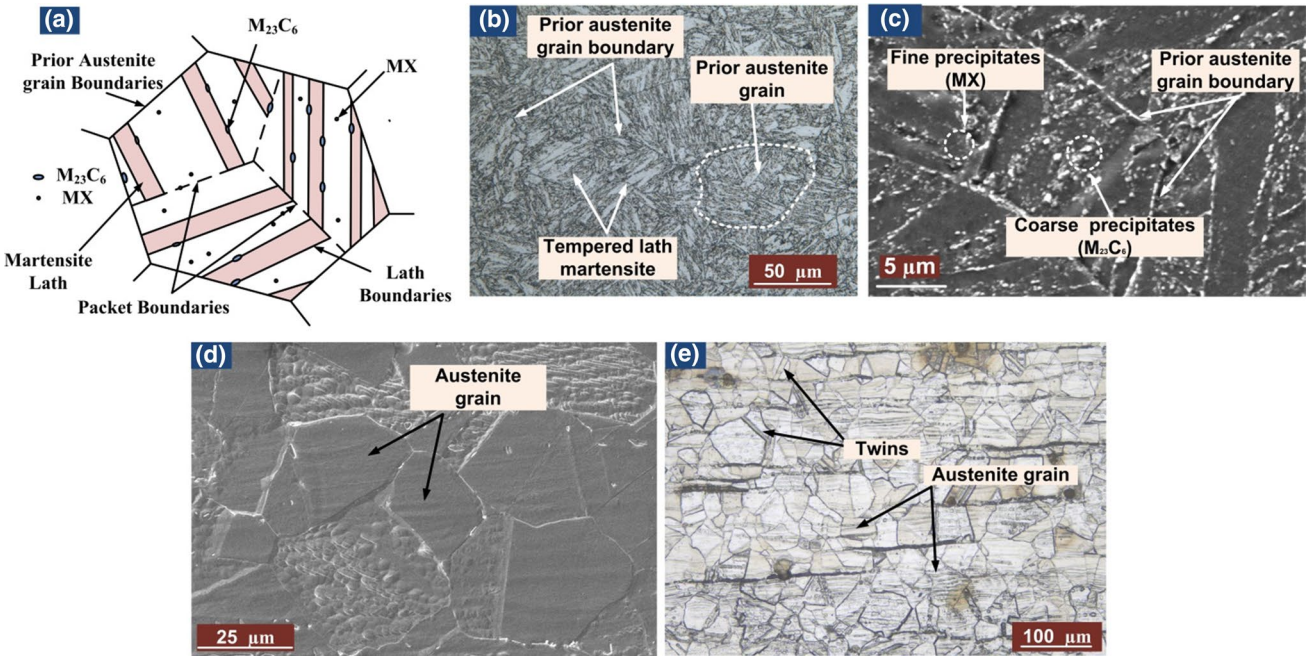

Fig. 1 **a** Schematic diagram of the prior austenite grain [27], **b** OM microstructure of the P92 BM, **c** SEM microstructure of the P92 BM, **d** SEM microstructure of the 304L SS BM and **e** OM microstructure of the 304L SS BM

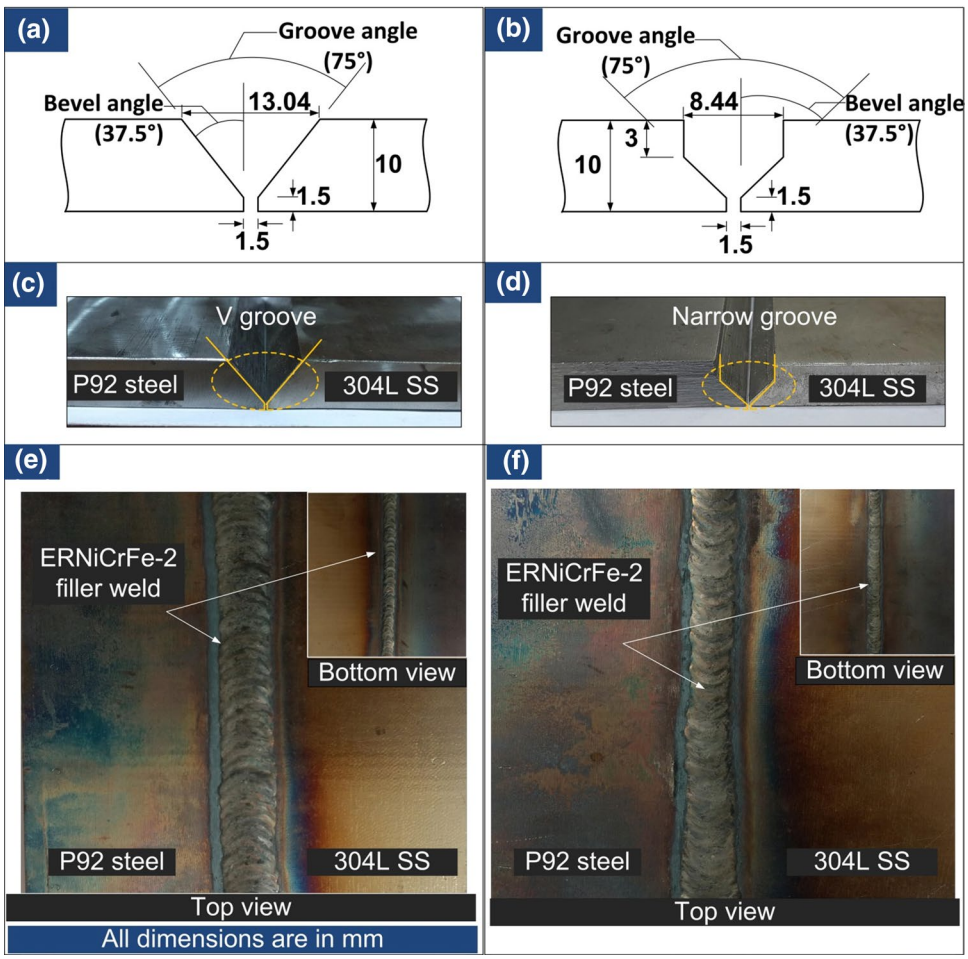

Fig. 2 **a**, **b** Schematic drawing of V-shape and Narrow shape groove profile, **c**, **d** V-shape and Narrow shape groove profile formed on P92 and 304L SS plate and **e**, **f** V-shape and Narrow shape groove profile TIG welded P92/304L SS DWJs

nickel-based ERNiFeCr-2 filler metal diameter of 2.4 mm. The manual TIG welding equipment (Model: Precision TIG 225) was used. The direct current electrode negative (DCEN) polarity was used with a tungsten-2% thoriated electrode. The non-variable welding process parameters were as follows: electrode diameter was 3.2 mm, the shielding gas was argon (99.995% purity), and the shielding gas flow rate was 14 L/min. In order to avoid the hot cracking of the DWJs, the P92 plate was pre-heated up to the temperature of 200–250 °C with the help of flame heating. The interpass temperature of 200 °C was maintained during the welding. The top and bottom view of the dissimilar welded plate is shown in Fig. 2e, f. The parameters for the welding were set by doing bead-on-plate weld trials. The welding parameters (such as current, voltage, and travel speed), heat input for each pass, and overall heat input considering 60% thermal efficiency for the GTAW process are provided in Table 3.

The OM and SEM examination specimens were prepared following the standard metallographic procedure given in ASTM standard E3-11. The specimens for various tests were extracted from the welded plate using a wire cut electrical discharge machine (WCEDM). The specimen for microstructure examination was prepared by performing a series of mechanical grinding operations using various SiC grit papers (#80 to #2000) and final polishing with 1 µm alumina slurry powder. The mirror polished specimen was then swabbed using a Villella's reagent solution (1 g picric acid + 5 ml concentrated HCL + 100 ml of ethanol) and left for 40–45 s to reveal the microstructure of the P92 base metal and P92 HAZ. The 304L SS side was swabbed using glyceregia (10 ml HNO_3 + 20 ml glycerol + 30 ml concentrated HCL) and left for the 50 s to reveal the twins, ferrite stringers, and polygonal austenite grains. The ERNiFeCr-2 weld fusion zone was electrolytically etched using 10% oxalic acid solution for (1.0 A/cm^2 current density; 6 V DC supply, 45 s exposure time) to reveal the microstructure. The stereo zoom microscope (Make: QUASMO, Model: SZB-45L) was used for macrostructure examination. The Image J software was used to measure macrostructure cross-sectional area, HAZ area, and HAZ width. The optical microscopy (OM) was performed on a Leica DMC4500 Optical microscope. SEM and energy dispersive spectroscopy (EDS) analysis was performed on Carl Zeiss EVO 18 scanning electron microscope. The tensile test specimens were prepared according to the dimensions given in the E8 standard. The tensile test was performed at room temperature according to the standard ASTM E8 at a 1 mm/min loading rate using a 100 kN capacity INSTRON 5980 universal testing machine. The Charpy V-notch impact toughness test was carried out on the sub-size 55 mm × 10 mm × 7.5 mm specimens. The Vickers microhardness examination was carried out using a semi-automatic microhardness tester at a load of 500 gf and a dwell time of 10 s. The schematic diagram of the various specimens prepared for metallography and mechanical testing is shown in Fig. 3.

Residual stress measurement was performed in an AW state and after PWHT to determine the longitudinal and transverse residual stress magnitude using the deep hole drilling (DHD) technique. The residual stress investigation is essential for P92/304L SS DWJs, as most of the failures occur due to the residual stress present in the component, as reported by various researchers [28, 29]. The DHD method was employed to evaluate the through-thickness welding induced residual stresses in the center of the weld fusion zone and the heat-affected zone of P92 and SS 304L in as-weld and PWHT conditions. The dissimilar metal welded plate prepared for residual stress study using the DHD technique is shown in Fig. 4. The DHD technique is a well-established experimental technique for measuring the welding-induced residual stresses. The DHD method is classified as a destructive method for measuring welding-induced

Table 3 Welding process parameters employed for P92/304L SS DWJs

Pass number	Welding parameters			Average heat input per unit length per pass (kJ/mm)	Total heat input per unit length of the weld (kJ/mm)
	Current (A)	Voltage (V)	Average welding Speed (mm/min)		
V-groove design parameters					
Root pass (1)	140	15.9	85	0.942	3.562
Filler pass (2)	130	15.5	80	0.907	
Capping pass (3)	130	15.5	80	0.907	
Backing pass (4)	130	15.5	90	0.806	
Narrow-groove design parameters					
Root pass (1)	140	15.9	98	0.818	3.11
Filler pass (2)	130	15.5	95	0.764	
Capping pass (3)	130	15.5	95	0.764	
Backing pass (4)	130	15.5	95	0.764	

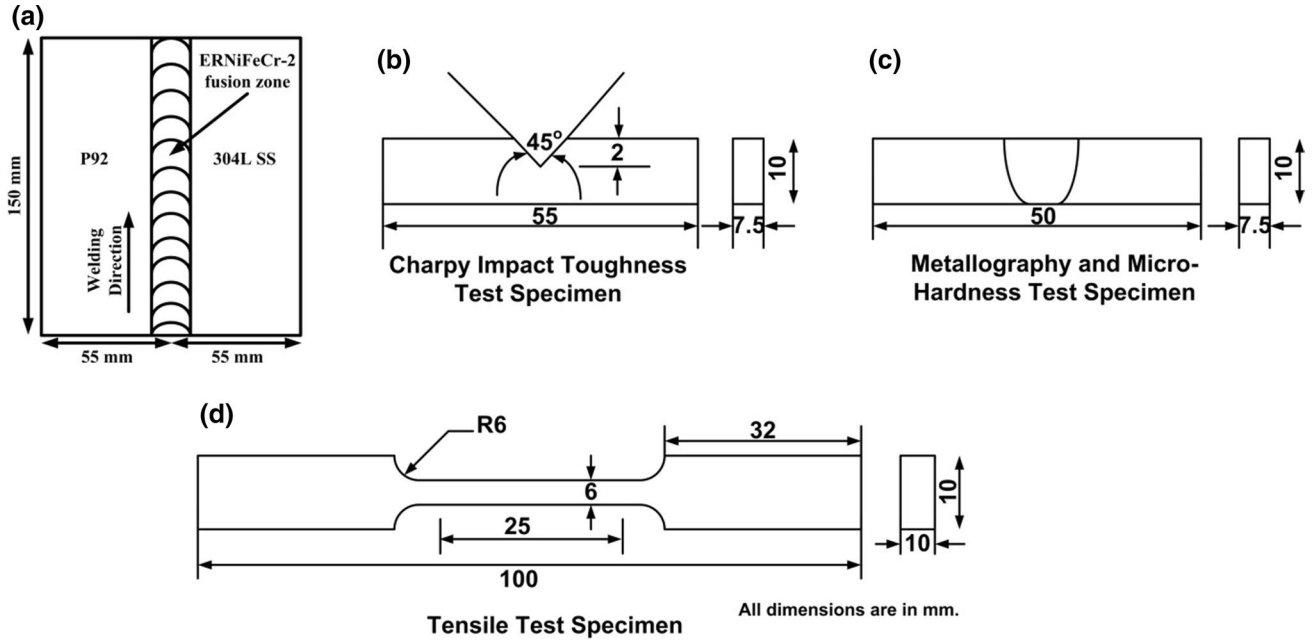

Fig. 3 **a** Schematic diagram of the P92/304L SS DWJs, **b** schematic diagram of the Charpy impact toughness test specimen, **c** schematic diagram of the metallography and micro-hardness test specimen and **d** schematic diagram of the tensile test specimen

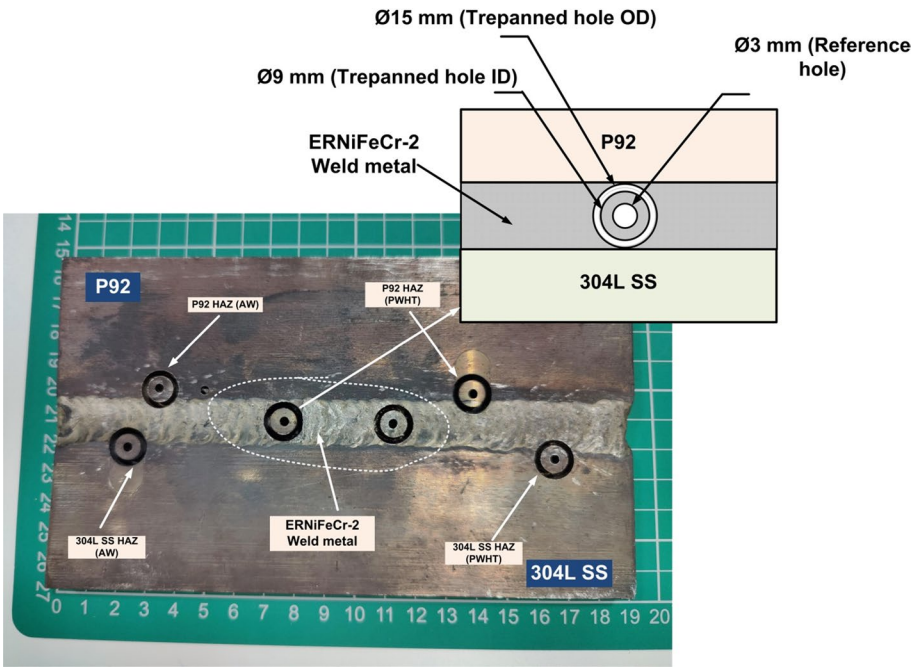

Fig. 4 P92/304L SS DWJs prepared for residual stress analysis using DHD technique

residual stresses. In this method, a small reference hole of diameter 3 mm is created with the help of the EDM tool. The DHD method involves the measurement of reference hole diameter before and after trepanning. Then in the next step, the diameter of this reference hole is measured with the help of an air probe system at various locations. In the third step, another hole of an internal diameter of 9 mm and outer diameter of 15 mm is coaxially trepanned using an EDM drilling machine. In the fourth step, the diameter of the reference hole is re-measured after trepanning. The change in reference hole diameter gives the value of the strain. The change in reference hole diameter is due to the stress relaxation that occurred due to material removal. This strain is then converted into stress using various analytical equations

[30]. Equations 1 and 2 were used to calculate the longitudinal and transverse ressolidification takes place.idual stress magnitudes. The ε_x and ε_y represent the strain in the longitudinal and transverse directions. The Δd_x represents the change in the diameter of the reference hole before and after trepanning.

$$\varepsilon_x = \frac{\Delta d_x}{d_x} = -\frac{1}{E}\left[3\sigma_x - \sigma_y\right] \tag{1}$$

$$\varepsilon_y = \frac{\Delta d_y}{d_y} = -\frac{1}{E}\left[3\sigma_y - \sigma_x\right] \tag{2}$$

3 Results and discussion

3.1 Macrostructure study

The macrograph displays the geometry of the weld bead and welding quality. The macrograph of the weld fusion zone and heat-affected zone of the P92-304L SS DWJs prepared using ERNiFeCr-2 filler is displayed in Fig. 5a, b. The macrograph shows a good fusion of the filler metal with the base metal. The high thermal conductivity of the P92 steel compared to the 304L stainless steel results in the formation of the broader HAZ toward the P92 side. Because of the low thermal conductivity of the 304L SS, negligible HAZ was formed towards the 304L side. Also, no macroscopic defects were observed from the macrograph. The various measurements were performed towards the HAZ and along the weld fusion zone. The HAZ width, weld fusion zone, and HAZ area for conventional V-groove and narrow groove design are listed in Table 4. Due to the higher thermal conductivity

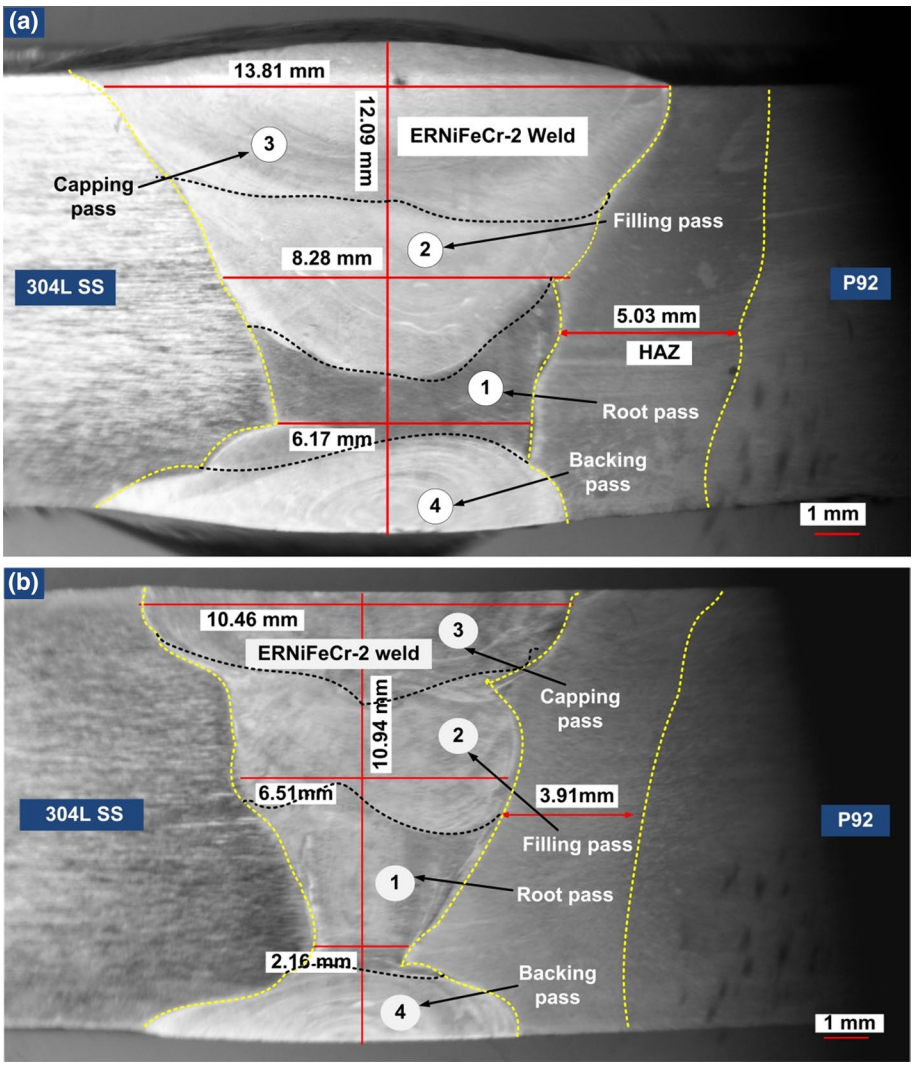

Fig. 5 Macrograph of the P92/304L SS DWJ for **a** V-groove DWJs and **b** narrow groove DWJs

Table 4 Weld fusion zone and HAZ area for conventional V-groove and narrow groove design

	Conventional V-groove	Narrow V-groove
Weld fusion zone area (mm^2)	87 ± 1	50 ± 1
HAZ area (mm^2)	38 ± 1	31 ± 1
HAZ width (mm)	5.03	3.91

of the P92 steel compared to the 304L SS, HAZ of width 5.03 mm for V-groove design and 3.91 mm for narrow groove design was recorded at the P92 side. The measured area of the weld fusion zone with reinforcement was 87 ± 1 mm^2 for the V-groove profile and 50 ± 1 mm^2 for the narrow groove profile. Thus, a narrow groove design helps in the minimization of the HAZ width and weld reinforcement area. From the macrostructure analysis, it can be concluded that the narrow groove design reduces the HAZ width and saves the costly nickel-based filler metal.

3.2 Microstructure study

3.2.1 Microstructure characteristics of P92 HAZ in as-weld state

The OM and SEM were employed to investigate the microstructure of the DWJs. The welding thermal cycle alters the microstructure of the base metal, resulting in the formation of the heat-affected zone (HAZ). This HAZ is further subdivided into various regions, as shown in Fig. 6a–d. Based on the microstructure characteristics, it can be sub-divided into CGHAZ, FGHAZ, and ICHAZ. The region adjacent to the fusion line is called CGHAZ. It is also known as the grain growth region. This region experiences a peak temperature (T_p) higher than the upper critical temperature ($T_p > > > Ac_3$) during the welding. At such a high temperature, precipitates that obstruct the growth of the austenite grains get dissolved. Thus grain boundaries become free from the precipitates, resulting in the formation of the coarse austenite grains. Also, the delta ferrite grain nucleates at such a high temperature ($T_p > 1250$ °C). The next region is called FGHAZ, also known as the grain refinement zone. This region experiences the peak temperature just above the upper critical temperature ($T_p > Ac_3$). This

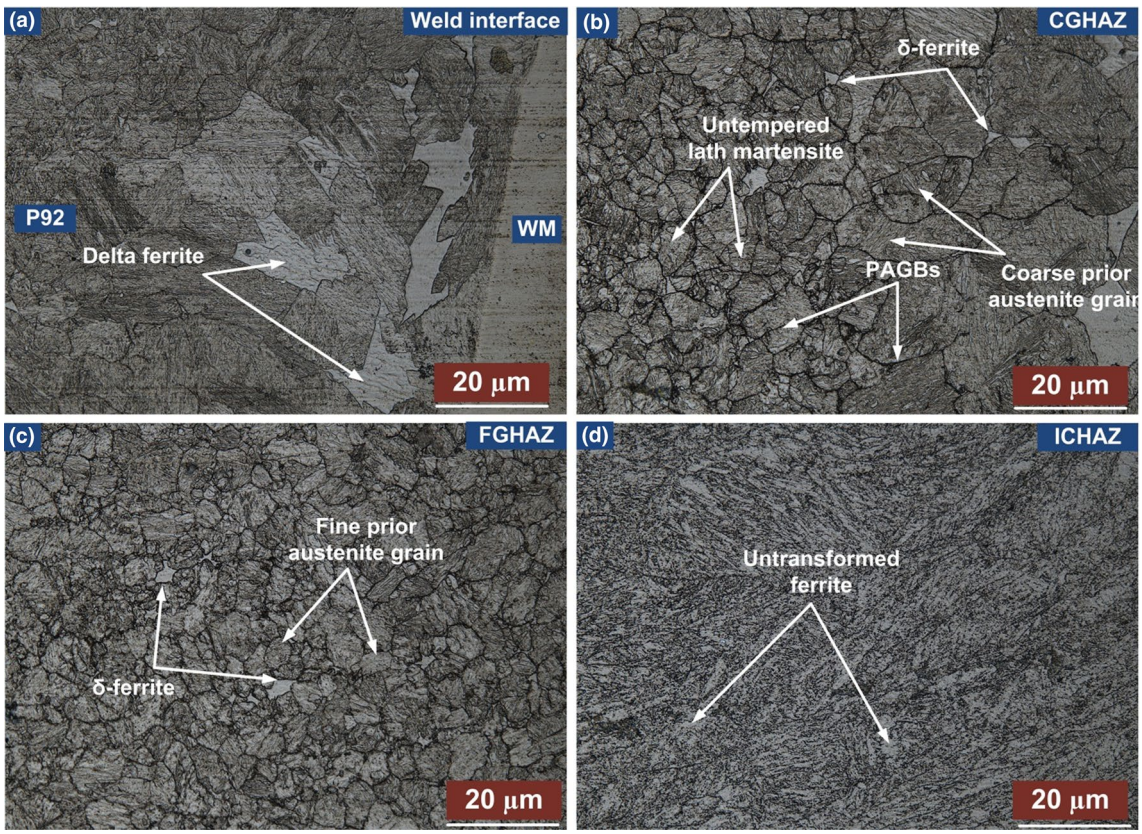

Fig. 6 In as-weld state optical microstructure of **a** weld and P92 HAZ interface, **b** CGHAZ, **c** FGHAZ and **d** ICHAZ for V-groove design

peak temperature is not sufficient to cause the complete dissolution of the precipitates. Thus, limited grain growth was observed in this region due to the obstruction by precipitates. It has been reported that the FGHAZ region is the weakest link in P92/304L DWJ during creep testing as most of the weldments fail from this region [31]. The next region is ICHAZ, which experiences the temperature between lower critical temperature and upper critical temperature ($Ac_1 < T_p < Ac_3$). At this temperature, partial dissolution of the precipitates and coarsening of the undissolved precipitates occur. Also, the new austenite grains can form, and the tempered austenite grains are tempered for a second time due to the weld thermal cycle. During cooling, both tempered and untempered martensite exists. The ICHAZ microstructure also shows the untransformed ferrite. This ferrite is generally alpha ferrite (α-Fe), and it is very soft in nature. This complex microstructure of the ICHAZ region formed due to the weld thermal cycle exhibits the lowest micro-hardness value among all the other regions due to the presence of soft alpha ferrite and is most susceptible to Type IV cracking. The region adjacent to the ICHAZ is known as the over-tempered base metal. This region experiences a temperature below the Ac_1, thus no microstructural changes occur due to the absence of phase transformation at this temperature, but tempering of the existing microstructure takes place. The formation of the CGHAZ, FGHAZ, and ICHAZ region, along with the formation of δ-ferrite, dissolution, and re-precipitation of the $M_{23}C_6$ and MX precipitates, can be well understood with the help of the phase diagram of P92 steel as shown In Fig. 7a, b. At a temperature above 1500 °C, the metal is completely in a liquid state. Below 1500 °C, when it starts to solidify, the formation of the coarse prior austenite grains (grain growth zone) and fine delta ferrite grain takes place. Below 1100 °C, the grain refinement takes place (fine grain zone). Between Ac_1 and Ac_3 temperature, the inter-critical heat-affected zone formation occurs. The formation of α-Fe below Ac_1 temperature is also shown in Fig. 7b. Below Ac_1 temperature and above 725 °C, the over-tempering of the base metal takes place. The over-tempering results in the further softening of the base metal matrix and thus reduces the hardness.

The SEM microstructure of the P92 HAZ in an as-weld state is illustrated in Fig. 8a–d. It shows the microstructure of the weld interface, CGHAZ, FGHAZ, and ICHAZ in an as-weld state. The microstructure consists of quenched (untempered) lath martensite inside the prior austenite grains and lath packets. Also, the δ-ferrite and soft zone near the weld interface was observed. The weld thermal cycle results in the dissolution of the precipitates. Some undissolved precipitates were observed in FGHAZ and ICHAZ. The grain size of the CGHAZ and FGHAZ in an as-weld state was observed as 15 ± 1 µm and 8 ± 1 µm, respectively.

Also, for the narrow groove profile, the OM and SEM image of the P92 HAZ in the as-weld state is shown in Figs. 9a–d and 10a–d. The soft zone and δ-ferrite were also observed for the narrow groove profile. It was decorated throughout the interface, as shown in intercept image Fig. 9a. In terms of the microstructure characteristic, no significant difference was observed between the two groove geometries. However, a negligible deviation in the grain size

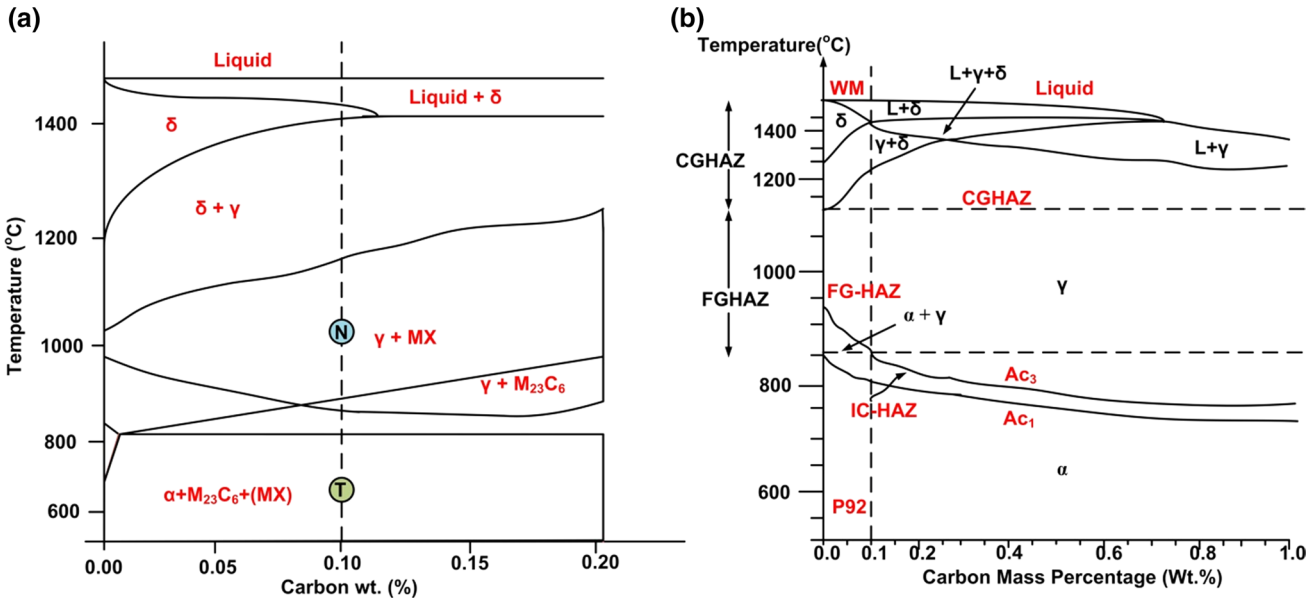

Fig. 7 **a** Phase diagram showing the evolution of $M_{23}C_6$ and MX precipitate during the normalizing and tempering and **b** equilibrium phase diagram of the P92 steel showing the formation of different HAZ regions with respect to temperature [32]

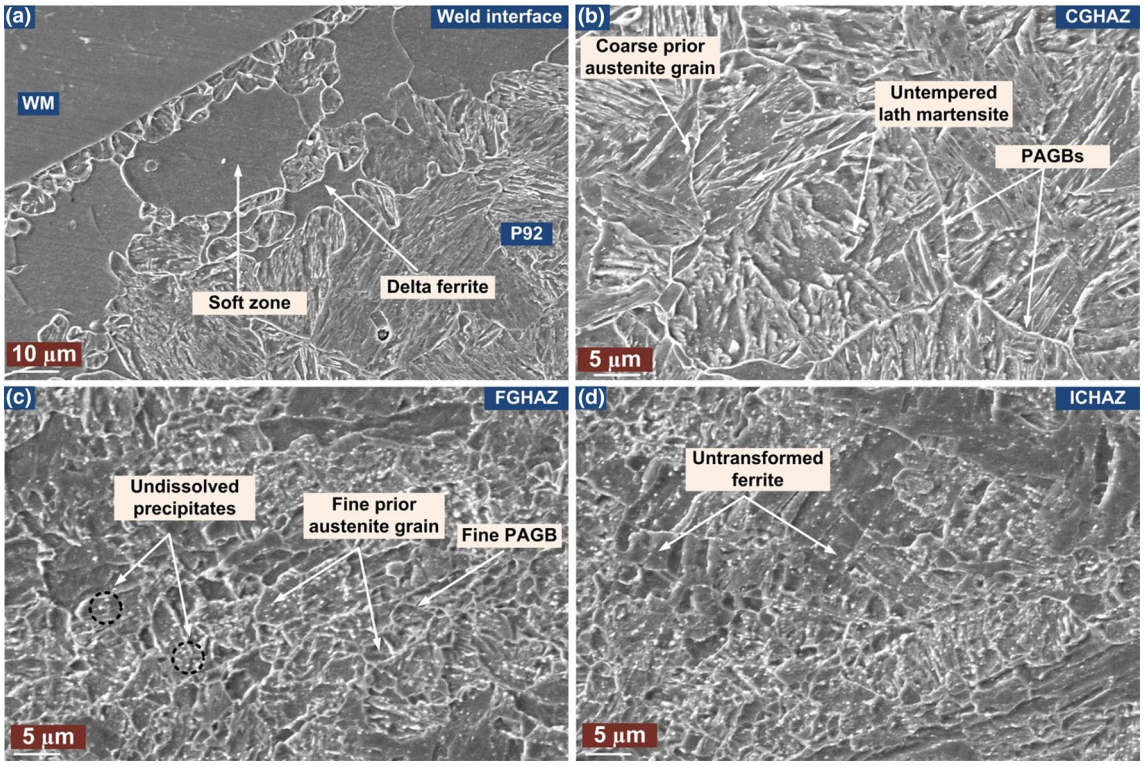

Fig. 8 In as-weld state SEM microstructure of **a** weld and P92HAZ interface, **b** CGHAZ, **c** FGHAZ and **d** ICHAZ for V-groove geometry

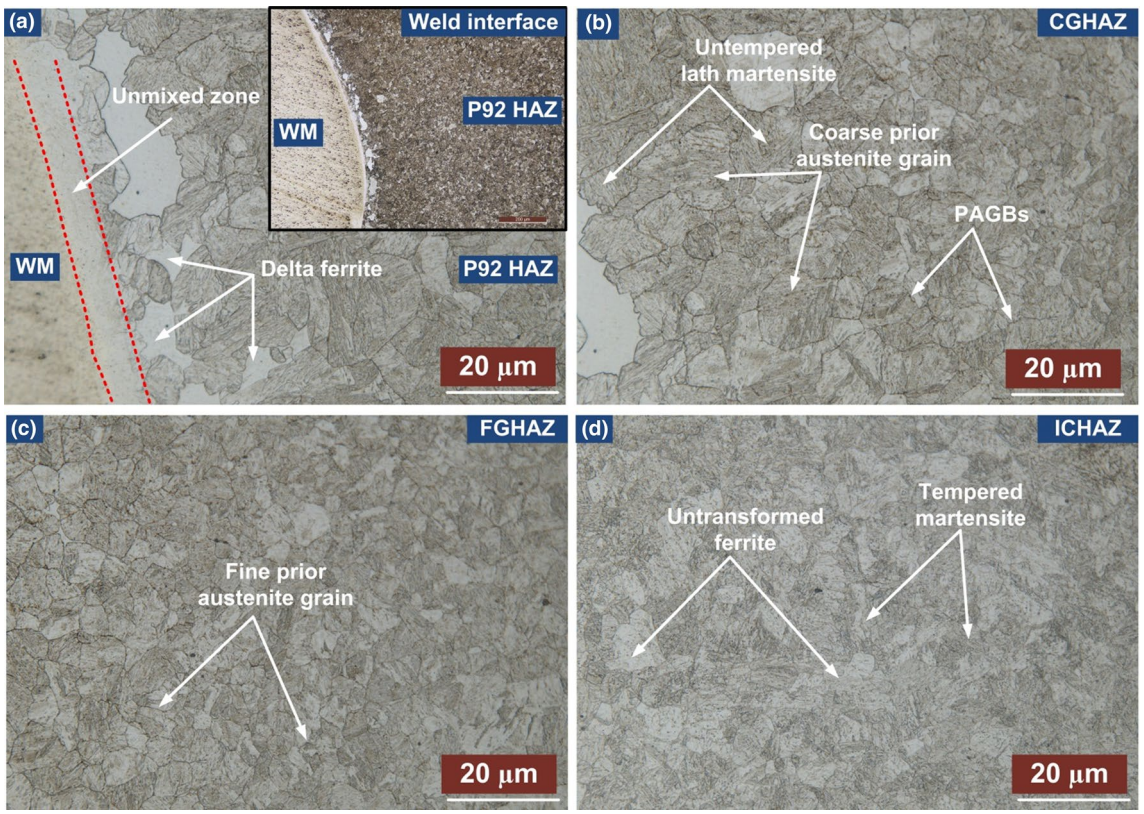

Fig. 9 In as-weld state optical microstructure of **a** weld and P92HAZ interface, **b** CGHAZ, **c** FGHAZ and **d** ICHAZ for narrow groove design

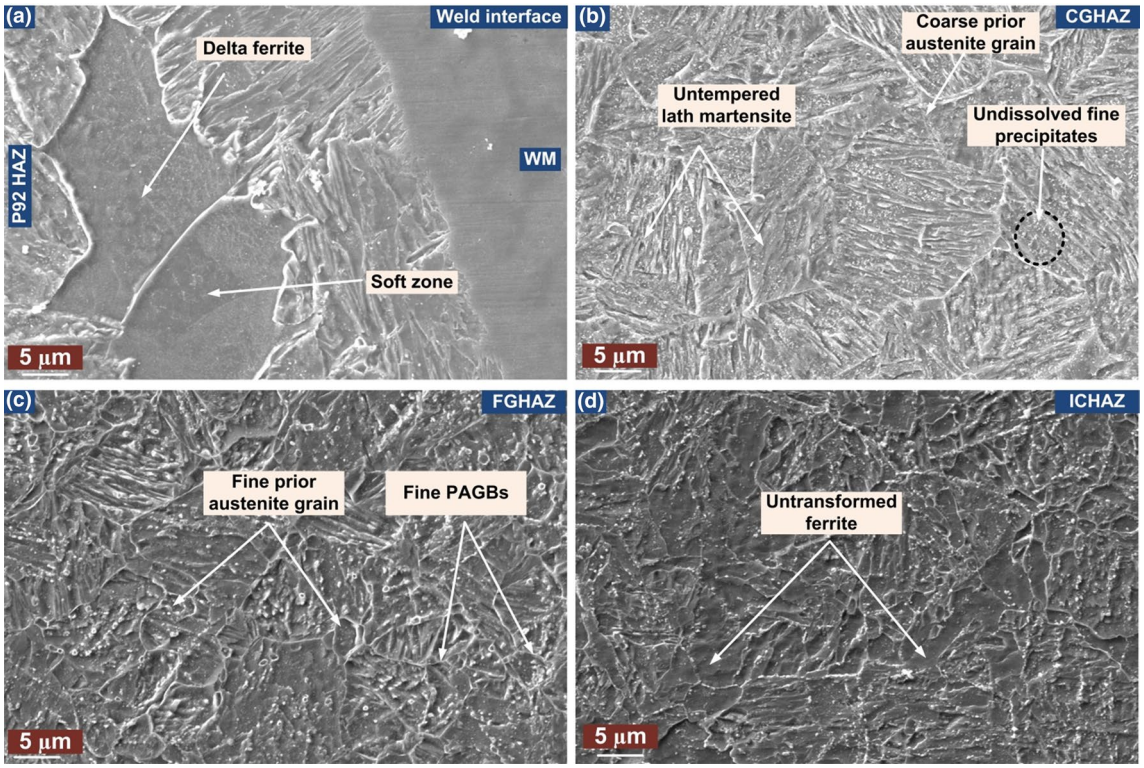

Fig. 10 In as-weld state SEM microstructure of **a** weld and P92HAZ interface, **b** CGHAZ, **c** FGHAZ and **d** ICHAZ for narrow groove design

was witnessed. The grain size of the CGHAZ and FGHAZ was observed as 12 ± 1 and 6 ± 1 µm, respectively.

3.2.2 Microstructure characteristics of ERNiFeCr-2 weld metal in as-weld condition

The fully austenitic microstructure of the ERNiFeCr-2 weld metal is depicted in Fig. 11a–i. The weld metal microstructure displays the dendritic grains, columnar dendrites, and cellular dendrites. The heat input and cooling rate affect the weld metal's microstructure morphology. The formation of the very fine equiaxed dendrites at the weld fusion zone and coarse columnar dendrites at the weld fusion boundary can be described based on thermal gradient (G) and cooling rate or growth rate (R). The degree of undercooling (temperature difference between the melting and solidification temperatures) is inversely proportional to the ratio G/R. The low G/R ratio forms the fine equiaxed dendritic structure, while the high G/R ratio forms the cellular dendritic structure [33]. The columnar dendritic structure at the weld fusion boundary is formed because of the steep thermal gradient at the fusion boundary. The thermal gradient at the weld center is not steeper, and also, the slow cooling rate at the weld center in the case of GTAW welding results in the formation of the fine equiaxed dendritic structure at the weld center [34]. The G/R ratio decreases from the fusion boundary to the weld pool interior. This results in the change of the solidification mode from columnar, cellular to equiaxed. The formation of the unmixed zone (UZ) like island, beach, and peninsula was also observed at weld metal and base material interface. The UZ is frequently formed during the dissimilar welding employing nickel-based filler due to the stagnant boundary layer's presence and the difference in the melting point and chemical composition between the base metal and filler metal [35]. Figure 12 displays the results of the SEM line mapping performed across the unmixed zone, i.e., island. The line map results show the variation of the nickel (Ni), chromium (Cr), and iron (Fe) elements across the island. The unmixed zone that exists in the form of an island was rich in Fe but deficient in Ni and Cr. Thus, it shows the inadequate mixing of the base metal with filler metal. The SEM image of the microstructure of the Inconel 718 weld metal is shown in Fig. 13a–i.

The ERNiFeCr-2 is a precipitation-strengthened superalloy. It has Ni_3Al type γ' precipitates and Ni_3Nb type γ'' precipitates. The Ni-based filler metal solidifies as a fully austenitic phase during the cooling after welding. The presence of niobium (Nb) elements makes the alloy susceptible to segregation during solidification. The segregation phenomenon takes place during the solidification of the nickel-based weld. The elements such as Fe, Ni, and Cr do not segregate during the solidification due to their high distribution

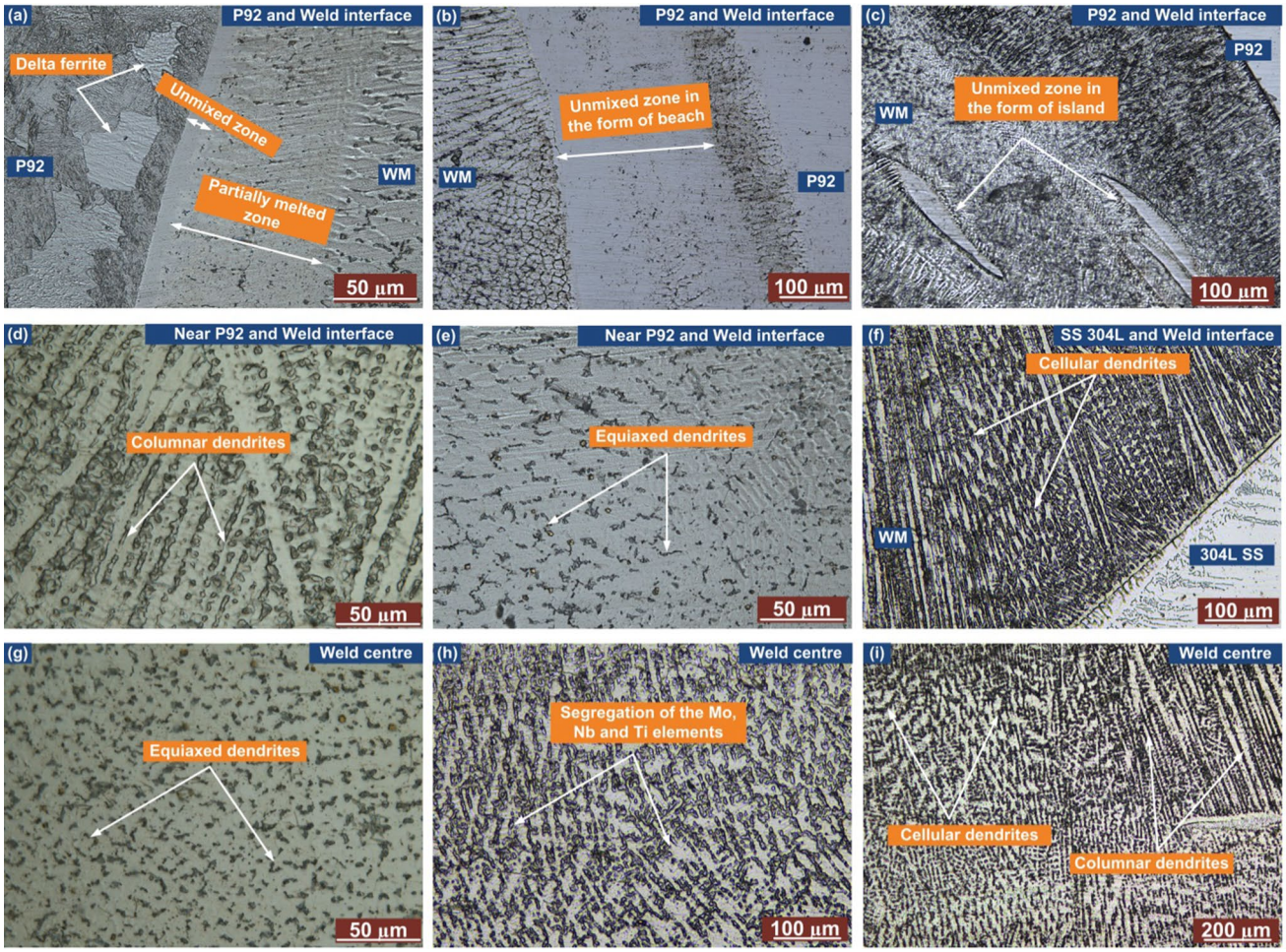

Fig. 11 In as-weld state optical microstructure of the ERNiFeCr-2 weld metal **a–c** P92 HAZ and weld interface for V-groove, **d**, **e** near P92 and weld interface, **f** 304L SS and weld interface, **g–i** weld center

coefficient (k) value ($k > 1$). The elements such as Mo, Nb, and Ti segregate during the solidification due to their low partition coefficient ($k < 1$). The Nb elements segregate during the solidification with more intensity than the Mo elements. Thus, segregation of the Nb elements during the solidification is primarily responsible for forming secondary phases [36]. The segregation of these elements results in the secondary phase formation, such as MoC, NbC, and TiC, as reported by various researchers [37]. In the present study, segregation of the Nb and Mo was also observed. The SEM area mapping of the secondary phase formed during the solidification of the ERNiFeCr-2 weld fusion zone is depicted in Fig. 14. The bright area in Fig. 14 shows a more concentration of the Mo and Nb elements, respectively. From the area mapping analysis, it can be concluded that possible precipitates may be MC-type (TiC or NbC or both), M_6C-type (M may be Fe, Mo, and Nb), and MoC-type.

The SEM–EDS technique was further employed to examine the quantitative distribution of the elements present in the secondary phases, as depicted in Fig. 15a–d. The region where the formations of the secondary phases occur because of the segregation of the Mo and Nb elements is known as the inter-dendritic region, while the region where the depletion of such elements takes place is known as the dendritic core. The EDS analysis indicated that the precipitates in the inter-dendritic region contain a higher amount of Mo and Nb than the matrix region. The formation of such a secondary phase is detrimental as it worsens the impact toughness of the weld metal [38]. The segregation of various alloying elements such as Mo and Nb during the solidification of ERNiFeCr-2 weld metal results in the formation of the eutectic type constituents and secondary phases that are not normally observed in the actual filler metal [39]. The microstructure characteristics of the ERNiFeCr-2 weld metal in the as-weld state were very much similar for both the V-shape and narrow groove profile. Figures 16a–f and 17a–f show the weld metal's OM and SEM microstructure for narrow groove

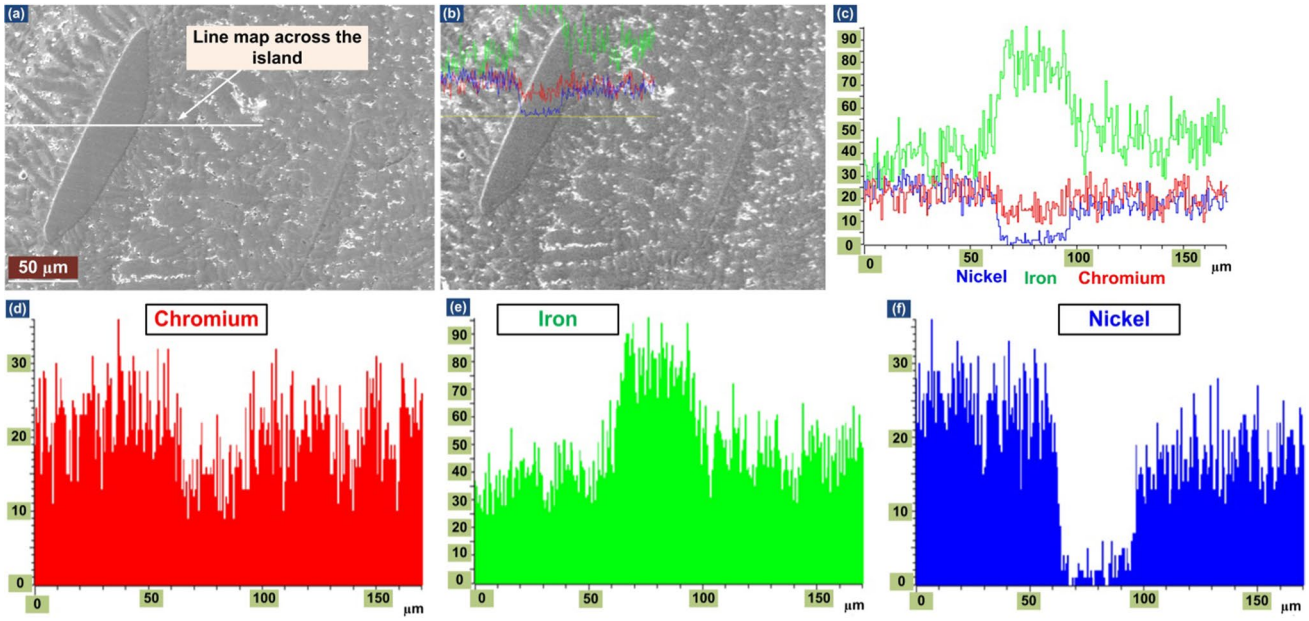

Fig. 12 Line mapping analysis across the unmixed zone formed in the form of island

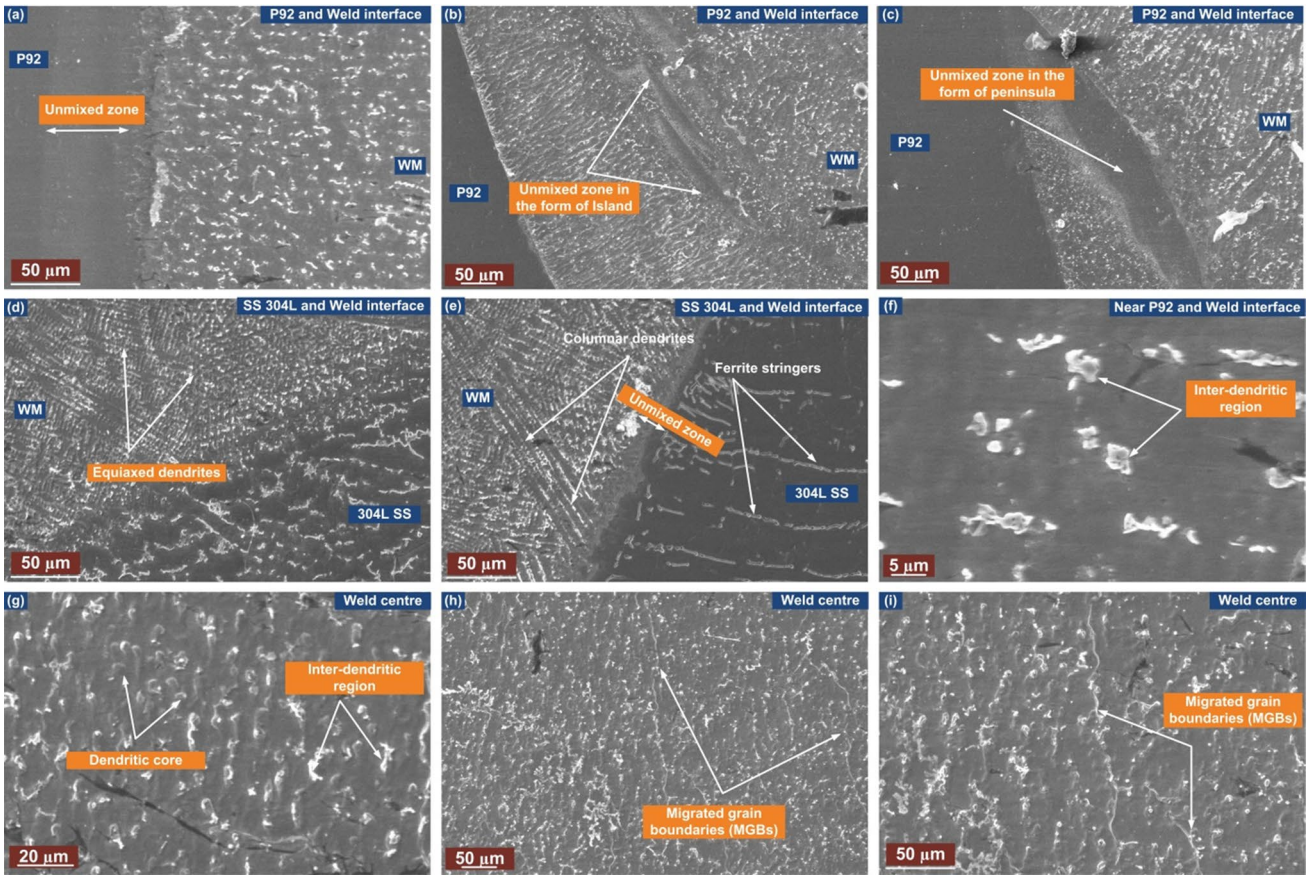

Fig. 13 In as-weld state SEM microstructure of the ERNiFeCr-2 weld metal for V-groove **a–c** P92 HAZ and weld interface, **d**, **e** 304L SS and weld interface, **f** near P92 and weld interface, **g–i** weld centre

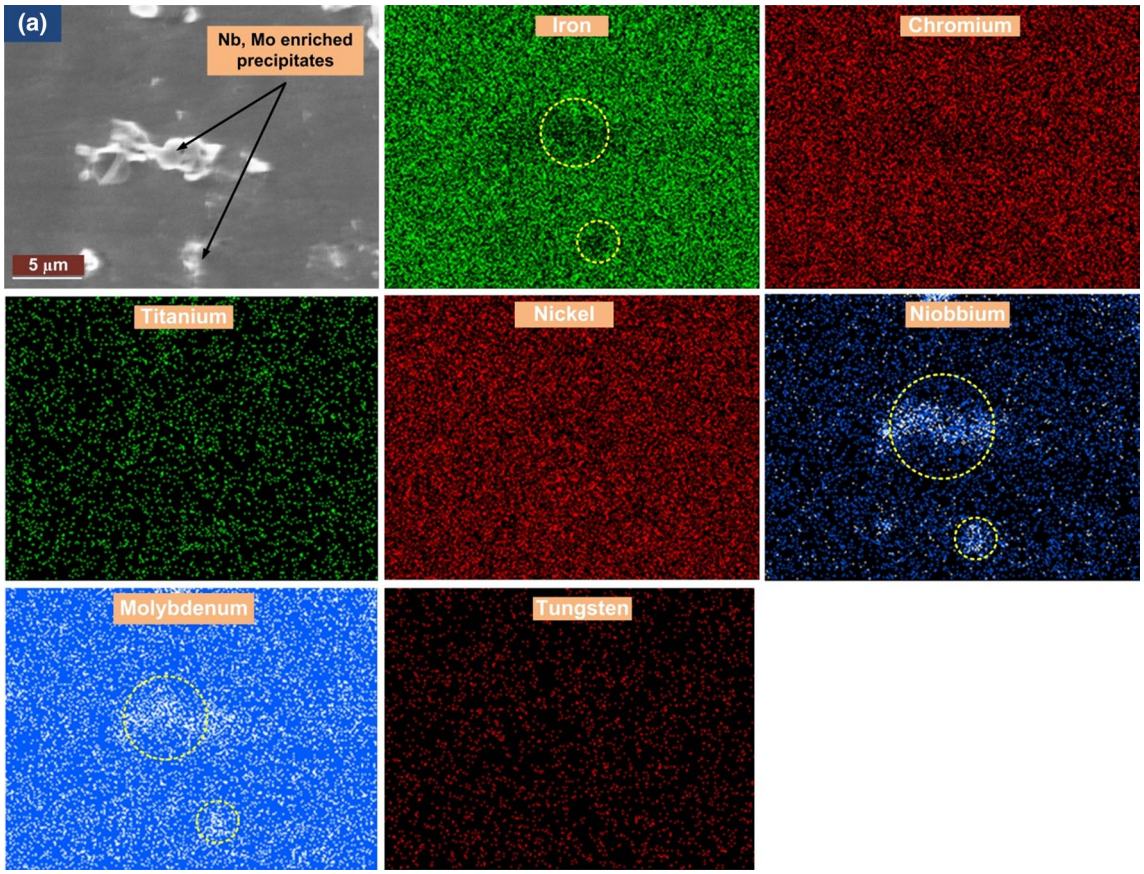

Fig. 14 SEM area mapping analysis indicating the Nb and Mo precipitation

geometry in an as-weld state. Also due to the segregation of Nb elements, the formation of laves phase may occur, as displayed in Fig. 17f. The segregation of Mo results in the formation of the Mo depleted zone, which makes the weld zone prone to corrosion [40]. It has been reported [41] that Nb-rich alloy solidifies through a three-step process.

(1) Primary solidification $L \rightarrow \gamma$,

(2) $L \rightarrow \gamma + NbC$,

(3) $L \rightarrow \gamma +$ Laves.

The chromium equivalents (Cr_{eq}) and nickel equivalents (Ni_{eq}) are used to identify austenitic, martensite, and ferritic phase stability. The modified Schaeffler formula [42] is given in Eqs. (3) and (4). The Cr_{eq} and Ni_{eq} calculated for P92 steel, 304L SS, and ERNiFeCr-2 weld according to the Schaeffler equation was (9.391, 3.305), (18.68, 9.16), and (25.59, 54.221), respectively. The corresponding Schaeffler diagram is shown in Fig. 18. The ratio of Cr_{eq} and Ni_{eq} is used to identify the mode of the solidification (austenitic or ferritic or both). For $Cr_{eq}/Ni_{eq} < 1.25$, the fully austenitic mode of solidification takes place [43]. For ERNiFeCr-2 weld metal, the ratio of Cr_{eq} and Ni_{eq} was found to be 0.472. Thus, for ERNiFeCr-2 weld metal fully austenitic mode of solidification takes place.

$$Cr_{eq} = Cr + 1.5\,(\%Mo) + 2\,(\%Si) + 5\,(\%V) + 5.5\,(\%Al) + 1.75\,(\%Cb) + 1.5\,(\%Ti) + 0.75(\%W) \quad (3)$$

$$Ni_{eq} = Ni + Co + 30\,(\%C) + 0.5\,(\%Mn) + 0.3\,(Cu) + 25\,(\%N) \quad (4)$$

3.2.3 Microstructure characteristics of 304L SS HAZ

The microstructure characteristics of the 304L SS HAZ are displayed in Fig. 19a–d. The microstructure near the weld interface was similar to that of the 304L SS BM. As discussed in the previous section, because of the low thermal conductivity of the 304L SS, the very thin HAZ formation takes place toward the 304L SS side. Also, no significant changes in the grain sizes and twins' characteristics were observed for 304L SS HAZ. Apart from the formation of ferrite stringers, no other significant microstructure

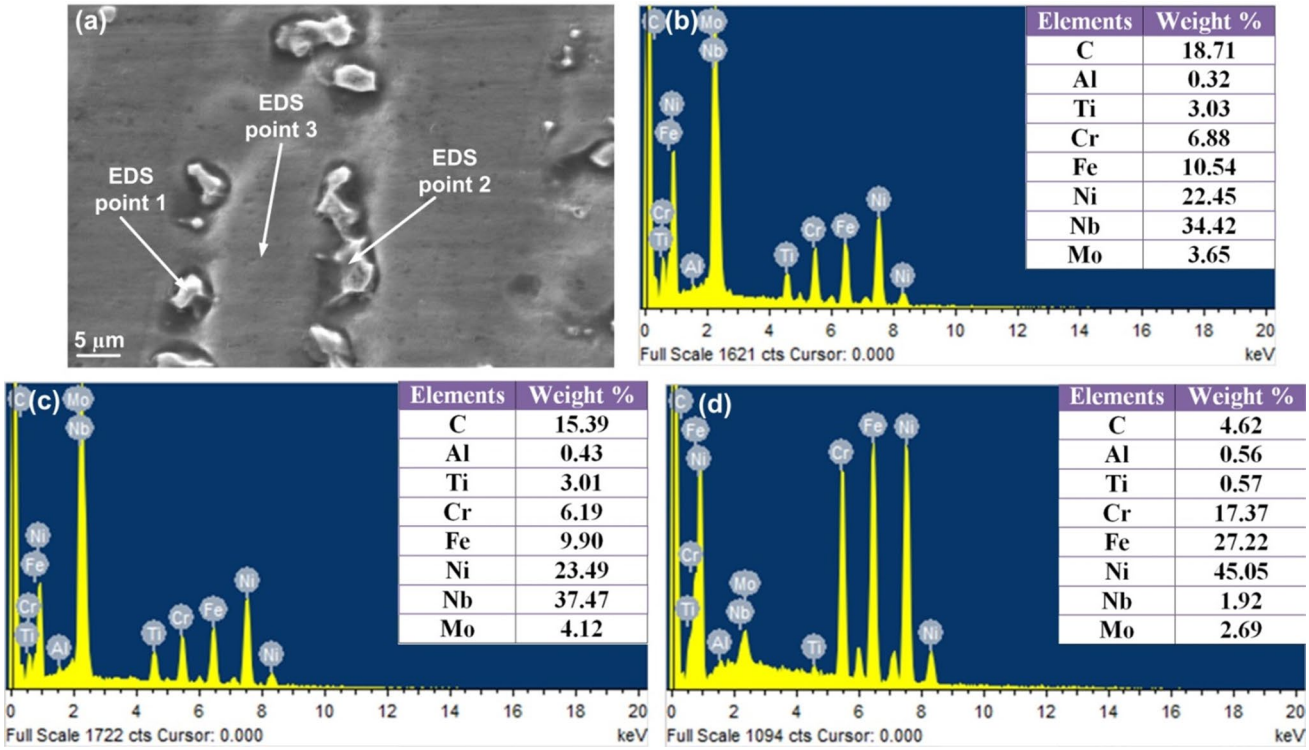

Fig. 15 EDS analysis at dendritic and inter-dendritic region **a** SEM image of the secondary phase, **b–d** EDS point analysis results of the location 1, 2, and 3, showing the segregation of the Nb and Mo

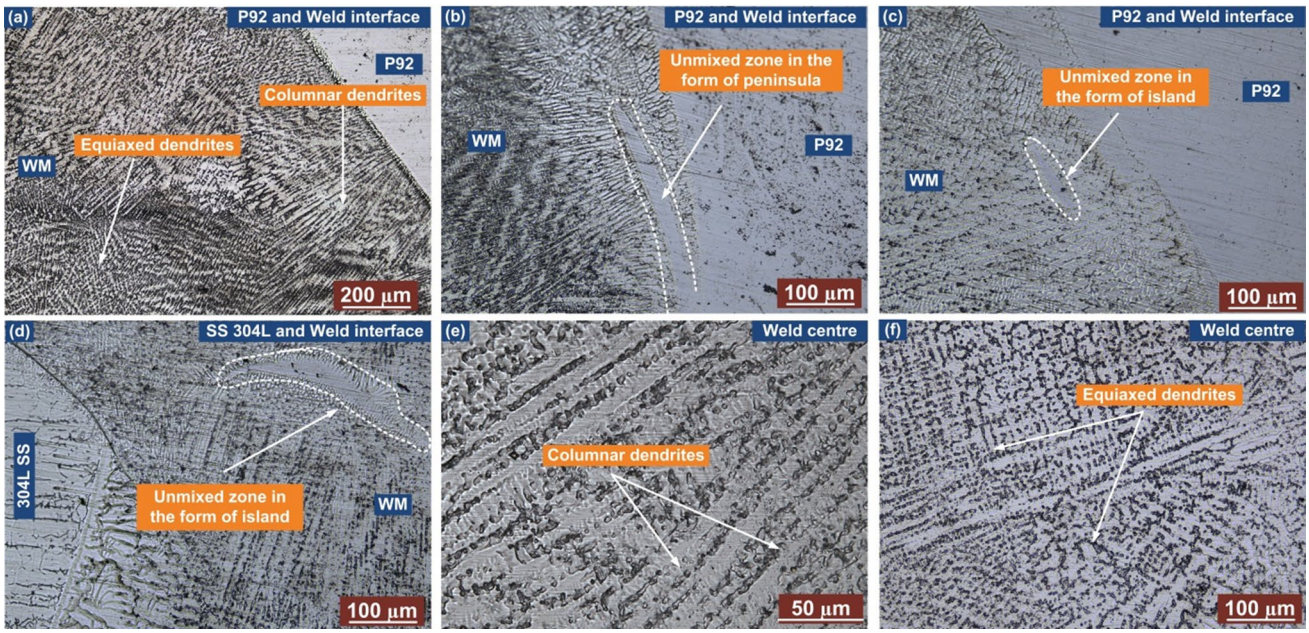

Fig. 16 In as-weld state optical microstructure of the ERNiFeCr-2 weld metal **a–c** P92 and weld interface, **d** 304L SS and weld interface and **e**, **f** weld centre for narrow groove design

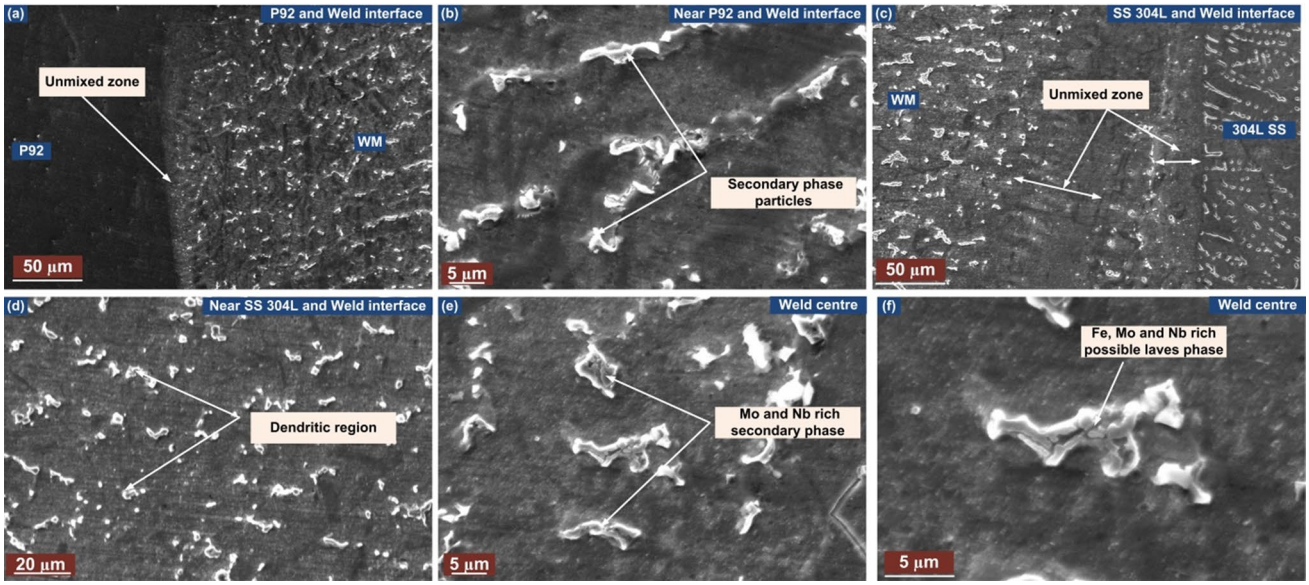

Fig. 17 In as-weld state SEM microstructure of the ERNiFeCr-2 weld metal **a** P92 and weld interface, **b** near P92 and weld interface, **c** 304L SS and weld interface, **d** near 304L SS and weld interface, **e**, **f** weld center for narrow groove

changes were observed for 304L SS HAZ. The EDS analysis was performed across the ferrite stringer, as depicted in Fig. 19c, d. The EDS result was as follows: Fe-67%, Cr-27%, Ni-4%, Mn, and Si-1%. The EDS result indicated the higher weight percentage of the chromium elements at the ferrite stringer compared to the base metal matrix. Thus, it can be confirmed that ferrite stringer is formed due to the segregation of the Cr elements. Thus, it can be concluded that heat produced during the weld thermal cycle has an insignificant effect on the microstructural features of 304L SS metal. From the micro-hardness examination also in the subsequent section, it can be confirmed that there was no substantial variation in the microstructure properties of the 304L SS after welding and PWHT. Thus, it can be said that 304L SS metal remains stable during the welding and after PWHT.

Fig. 18 Schaeffler diagram

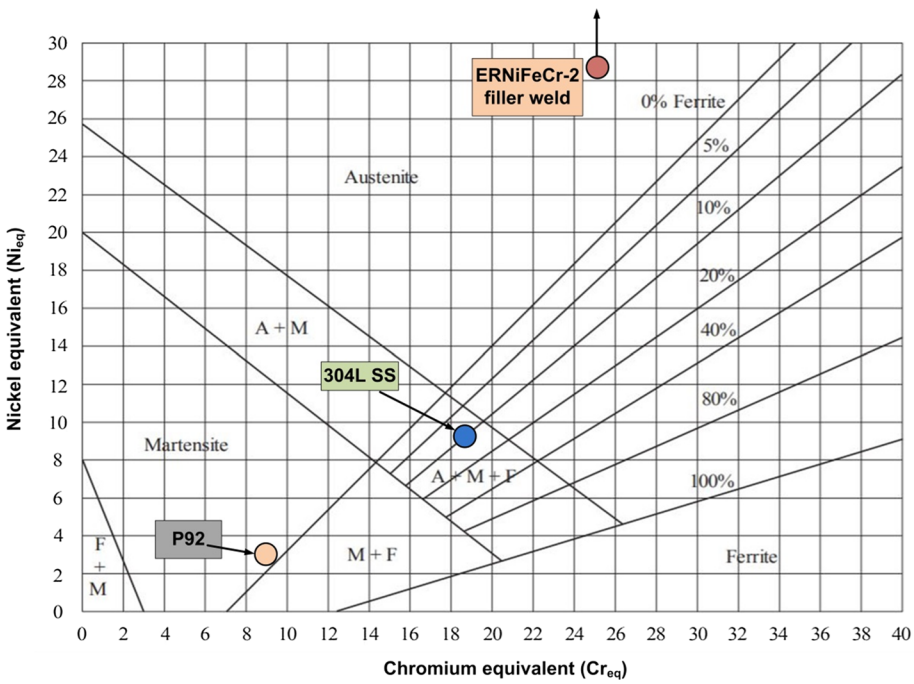

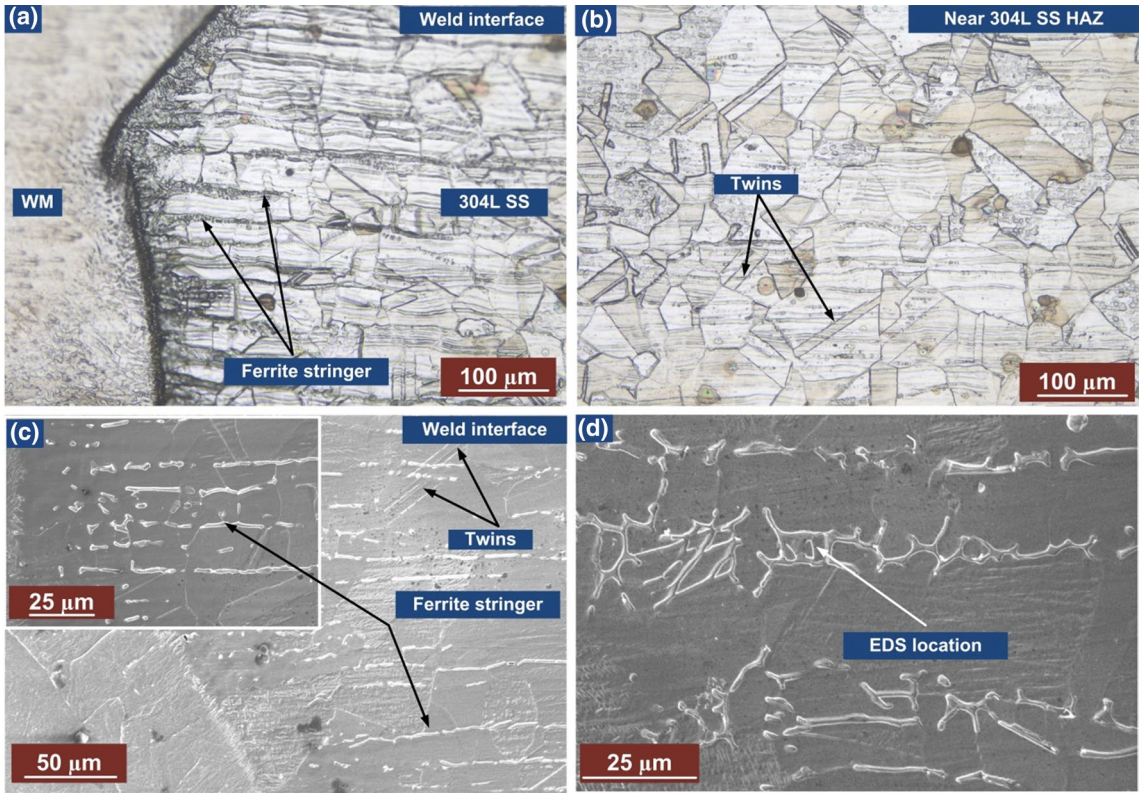

Fig. 19 **a**, **b** OM micrograph of the 304L SS HAZ and weld interface and **c**, **d** SEM micrograph of the 304L SS HAZ and weld interface

3.2.4 Microstructure characteristics of P92 HAZ after PWHT

The weld thermal cycle leads to drastic mechanical property variation and forms undesirable microstructure in the HAZ region. The ferritic/martensitic P92 steel DWJs are always subjected to PWHT after welding to temper the martensite, re-precipitation of the precipitates dissolved during the welding, and to relieve the residual stresses. The PWHT is necessary for the P92/304L SS DWJs to improve the mechanical properties and relieve the residual stresses developed during the welding. The microstructure of the P92 HAZ after PWHT is shown in Fig. 20a–d. The prior austenite grain boundary, lath, and block boundaries decorated with $M_{23}C_6$ and MX precipitates were observed after PWHT, as shown in Fig. 21a–d. The SEM images show the microstructure of the weld interface, CGHAZ, FGHAZ, and ICHAZ after PWHT. The PWHT result in the evolution of the precipitates dissolved during the weld thermal cycle. These precipitates are required for the creep strength and high-temperature tensile strength of the P92 steel. Also, the formation of the soft zone near the weld interface was observed. The δ-ferrite was stable after PWHT. The soft zone is formed at the interface due to the carbon migration from the low Cr metal side toward the high Cr metal. The Ni-based filler restricts the carbon migration from ferritic steel toward the nickel-based weld metal. Thus, carbons are depleted at the interface and form a carbon-depleted zone (CDZ), also known as the soft zone near the fusion line. The other microstructure variation is the formation of the delta ferrite. Sakthivel et al. [22] reported that the size of the $M_{23}C_6$ precipitates was very high in the ICHAZ region compared to the CGHAZ and FGHAZ. The coarsening of the $M_{23}C_6$ precipitates occurs during the welding and after PWHT. The finer precipitates obstruct the movement of the dislocations more effectively than the coarse precipitates. Also, in the ICHAZ region, boundaries are generally free from the $M_{23}C_6$ precipitates due to the partial transformation to austenite. This undesirable microstructure characteristic of the ICHAZ region makes it most susceptible to premature failure from the ICHAZ region during the service. Also, this complex microstructure is responsible for the low microhardness value of the ICHAZ region. Figures 22a–d and 23a–d show the OM and SEM microstructure of the P92 HAZ after PWHT for narrow groove geometry DWJs.

3.2.5 Microstructure characteristics of ERNiFeCr-2 weld metal after PWHT

The microstructure characteristics of the ERNiFeCr-2 weld metal after PWHT were very much similar for both the

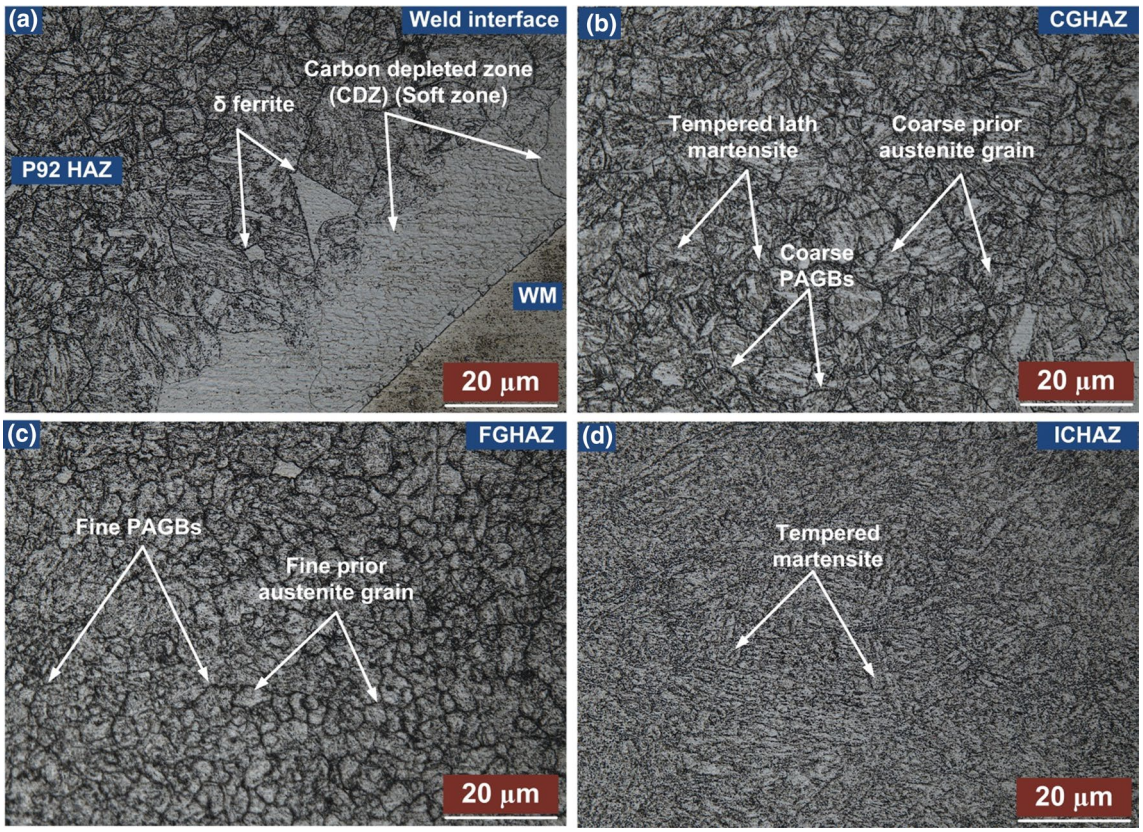

Fig. 20 After PWHT, optical microstructure of **a** weld and P92HAZ interface, **b** CGHAZ, **c** FGHAZ and **d** ICHAZ for V-groove design

V-shape and narrow groove profile. The ERNiFeCr-2 is a nickel-based super alloy strengthened by γ″ (Ni_3Nb), and γ′ (Ni_3Al) precipitates. But, during solidification, the Nb segregate and strengthening effect of these Nb rich precipitates reduces. Also, the formation of laves phase in weld metal becomes easier due to the micro-segregation of Mo, Nb, and Ti elements. Thus, the segregation of Nb elements results in the loss of the mechanical properties of the weld metal. The ERNiFeCr-2 filler metal has excellent mechanical properties and corrosion resistance at elevated temperatures. The presence of Ni (52.70%) and Cr (17.39%) along with Nb, Mo, and Ti enable its response to hardening by heat treatment [44]. Figures 24a–f and 25a–h show the OM and SEM microstructure of the weld fusion zone after PWHT for V-groove geometry. The microstructure analysis shows that not much change in microstructural features was found after PWHT. The UZ, secondary phases, and dendritic region were observed even after PWHT. Figures 26a–f and 27a–f show the OM and SEM microstructure of the weld fusion zone of narrow groove DWJs after PWHT. Apart from the secondary phases, the Laves phase was also observed due to the segregation of Mo and Nb. The presence of Fe in the austenitic matrix further promotes the precipitation of Laves phase. The SEM line mapping and EDS analysis were performed at the weld and base metal interface (mainly in the UZ) to identify the variation of the key alloying elements in these critical regions. The SEM line mapping and EDS analysis performed across the P92/ERNiFeCr-2 weld interface are shown in Figs. 28 and 29. The SEM line mapping and EDS analysis performed across the 304L SS/ERNiFeCr-2 weld interface are shown in Figs. 30 and 31. The line mapping result shows the significant variation of the various elements like chromium (Cr), nickel (Ni), and iron (Fe) at the interface. The line mapping examination indicated that the interface (unmixed zone) has a different amount of the Cr, Ni, and Fe elements than the bulk weld metal and adjacent base metal. The EDS analysis at the weld and base metal interface also indicated the variation in the Cr, Ni, and Fe elements compared to the bulk weld metal and adjacent base metal.

3.3 Micro-hardness testing

The microhardness measurement was carried out to analyze the variation in the microhardness value across the fusion zone, unmixed zone, base materials, and heat-affected region. The horizontal distribution of the micro-hardness for P92-ERNiFeCr-2-304L SS DWJs of V-shape and narrow

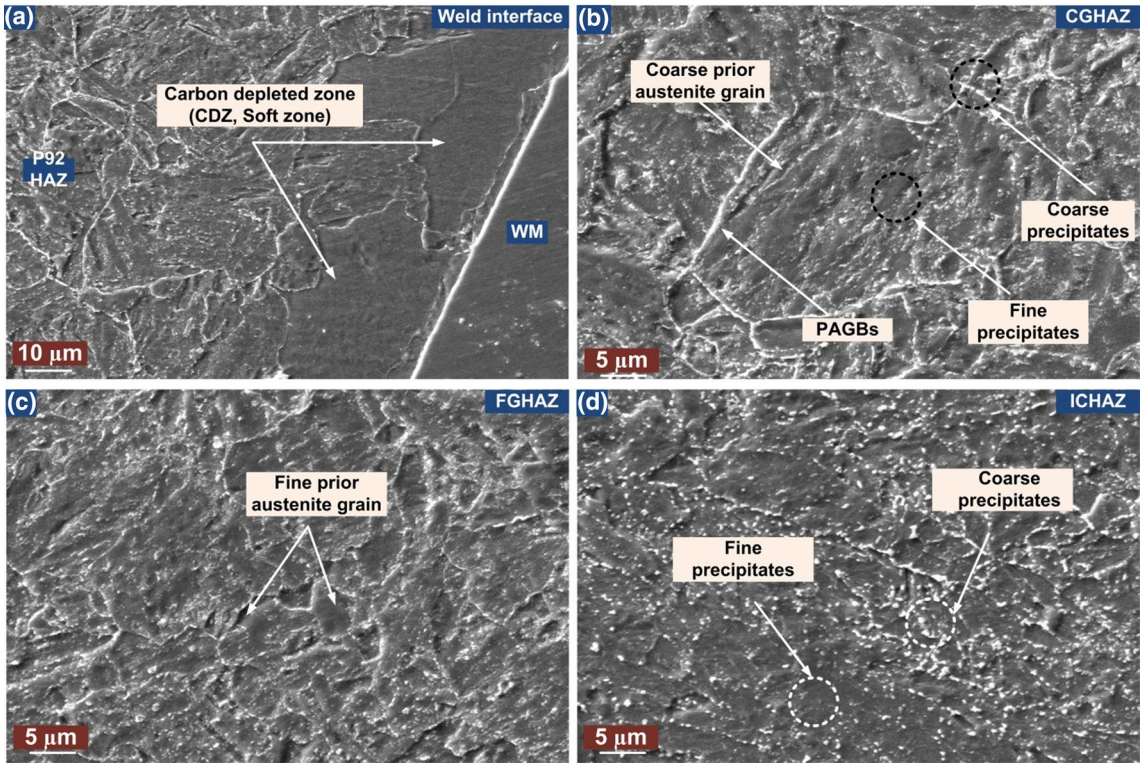

Fig. 21 After PWHT, SEM microstructure of **a** weld and P92HAZ interface **b** CGHAZ **c** FGHAZ and **d** ICHAZ for V-groove design

shape grove profile is shown in Figs. 32a, b and 33a, b. The distance between each indentation was 1 mm (distance was reduced to 0.5 mm for P92 HAZ to get the precise value of the microhardness for CGHAZ, FGHAZ, and ICHAZ). The micro-hardness profile was plotted using OriginPro 8. The hardness of the weld fusion zone in the as-weld situation was lower than in the PWHT situation. The low hardness value of the weld fusion zone may be due to the segregation of the Nb element during the welding process. The segregation of the Nb element results in the less amount of the Nb available for the formation of the γ″{Ni_3(Nb)} precipitates. The segregation of the Nb elements results in the loss of the strengthening effect of the γ″ precipitates. The hardening recovery was observed for the ERNiFeCr-2 weld fusion zone after PWHT. After PWHT, the micro-hardness of the weld fusion zone was increased. It is because the precipitates that were dissolved during the weld thermal cycle tend to precipitate again due to prolonged exposure at high temperatures. After PWHT, limited recovery in the strength and hardness was observed for the ERNiFeCr-2 weld zone. The ERNiFeCr-2 (Inconel 718) is precipitation strengthened Ni-base alloy. Thus it can be assumed that PWHT at 760 °C, 2 h, which was mainly performed to improve the properties of P92 steel, may alter the properties of the ERNiFeCr-2 weld up to a certain extent. The PWHT, known as low-temperature anneal in the range from 955 to 1010 °C is recommended for precipitation hardened Inconel 718 alloy to restore the weld strength by precipitation and to ensure fine grain size [39]. The indentation was also taken in the lateral direction of the weld fusion zone. The micro-hardness variation along the root to the weld cap is shown in Figs. 32c and 33c. The variation in the hardness value was found because of the tempering effect of the subsequent passes and the segregation of the Nb and Mo elements in the inter-dendritic region. It was also observed from the micro-hardness measurement across the weld fusion zone that columnar dendritic grain structure has a high micro-hardness value (~±305HV0.5), cellular dendritic grain structure has a moderate micro-hardness value of (~±270HV0.5), and equiaxed dendritic grain structure has the lowest micro-hardness value of (~±235HV0.5).

Regarding the P92 HAZ, the CGHAZ was the region with the highest micro-hardness value (456HV0.5 for V-groove design and 445HV0.5 for narrow groove design) (Table 5) in as-weld condition. The high microhardness value of the CGHAZ was associated with the formation of the quenched martensite and the dissolution of the precipitates. The peak temperature for P92 CGHAZ is higher than the dissolution temperature of the $M_{23}C_6$ precipitates leading to the complete dissolution of these precipitates. The dissolution of these precipitates leads to a higher amount and C and N elements in the CGHAZ region. This causes the high micro-hardness of the CGHAZ region. Thus CGHAZ

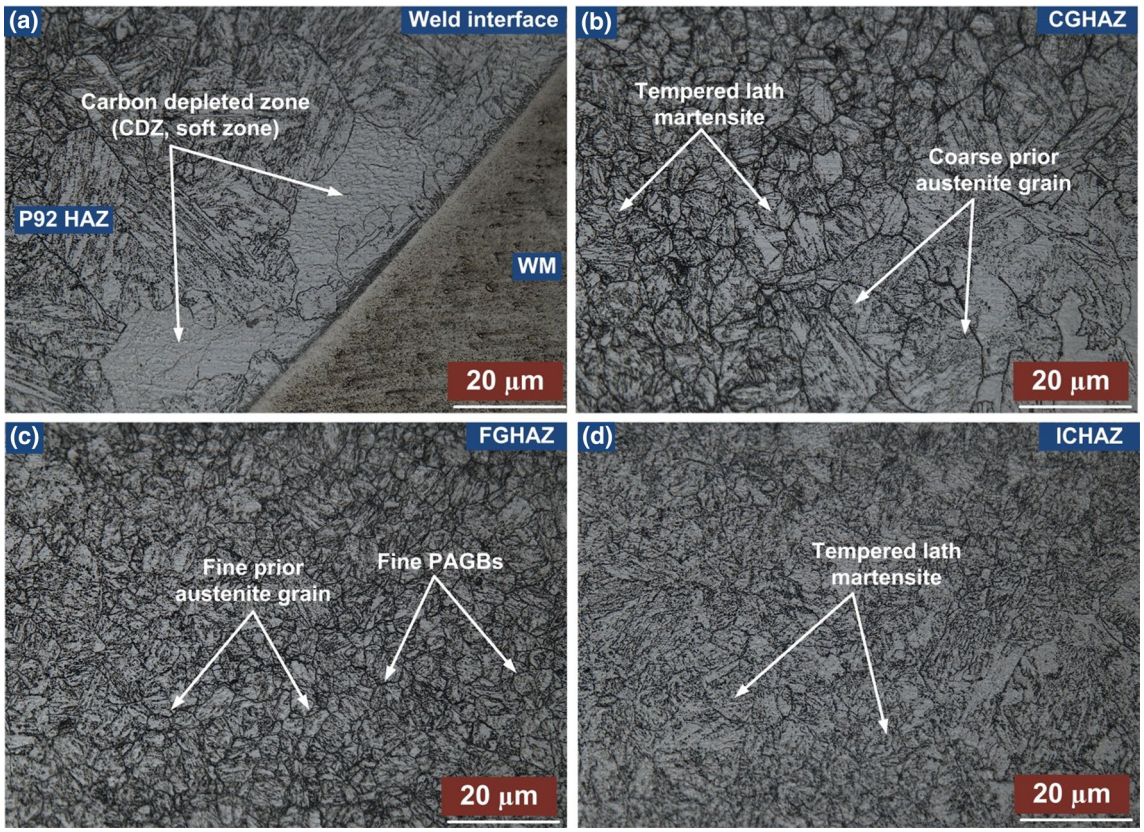

Fig. 22 After PWHT, optical microstructure of **a** weld and P92HAZ interface **b** CGHAZ **c** FGHAZ and **d** ICHAZ for narrow groove design

region features the highest micro-hardness value among all the other regions. Kulkarni et al. [45] observed the micro-hardness value of the CGHAZ region as ~453HV0.5. They reported that the high micro-hardness value of the CGHAZ region is due to the formation of high carbon martensite. The FGHAZ region features a comparatively low micro-hardness value (375HV0.5 for V-groove design and 360HV0.5 for narrow groove design) (Table 5) than the CGHAZ region because of the survival of the $M_{23}C_6$ and MX precipitates due to the low temperature experienced during the weld thermal cycle. Thus, fewer C and N weight percentages are present in the matrix of FGHAZ. The hardness of the P92 CGHAZ and FGHAZ was decreased after PWHT due to the tempering of the quenched martensite produced during the cooling after welding. Saini et al. [46] reported that a significant reduction in the micro-hardness value after the PWHT is due to the softening of the martensite and the evolution/growth of the precipitates. The low micro-hardness value of the ICHAZ region in AW state and after PWHT was due to the detrimental microstructure formed during the welding. A similar kind of micro-hardness variation was reported by Shin et al. [31] during the dissimilar joining of P92 steel with Inconel 740H. They also observed the peak micro-hardness value at CGHAZ, followed by FGHAZ, and the minimum micro-hardness value at ICHAZ (Table 5). The microhardness profile indicated that 304L SS has a similar magnitude of hardness before and after PWHT.

The micro-hardness magnitude at several other important locations, which are difficult to identify from the graph, is shown in Fig. 34. The micro-hardness of the delta ferrite grain, unmixed zone, and the soft zone is depicted in Fig. 34. The micro-hardness of the soft zone was recorded as ~ ±200HV0.5. The micro-hardness of the delta ferrite zone was recorded as ~ ±190HV0.5. The low micro-hardness of 154HV0.5 and 196HV0.5 has been reported for δ-ferrite [47]. The micro-hardness of the unmixed zone formed at the P92 side was recorded as ~ ±227HV0.5, which was very close to the micro-hardness value of the P92 base metal. The micro-hardness of the unmixed zone formed at the 304L SS side was recorded as ~ ±190HV0.5, which is very close to the micro-hardness value of the 304L SS base metal.

3.4 Tensile strength of the welded joints

The tensile test was performed on as-weld and PWHT P92/304L SS DWJs samples. Figure 35a, b shows the fracture specimen with the fracture location of the DWJs specimens, and Fig. 35c shows the stress–strain behavior

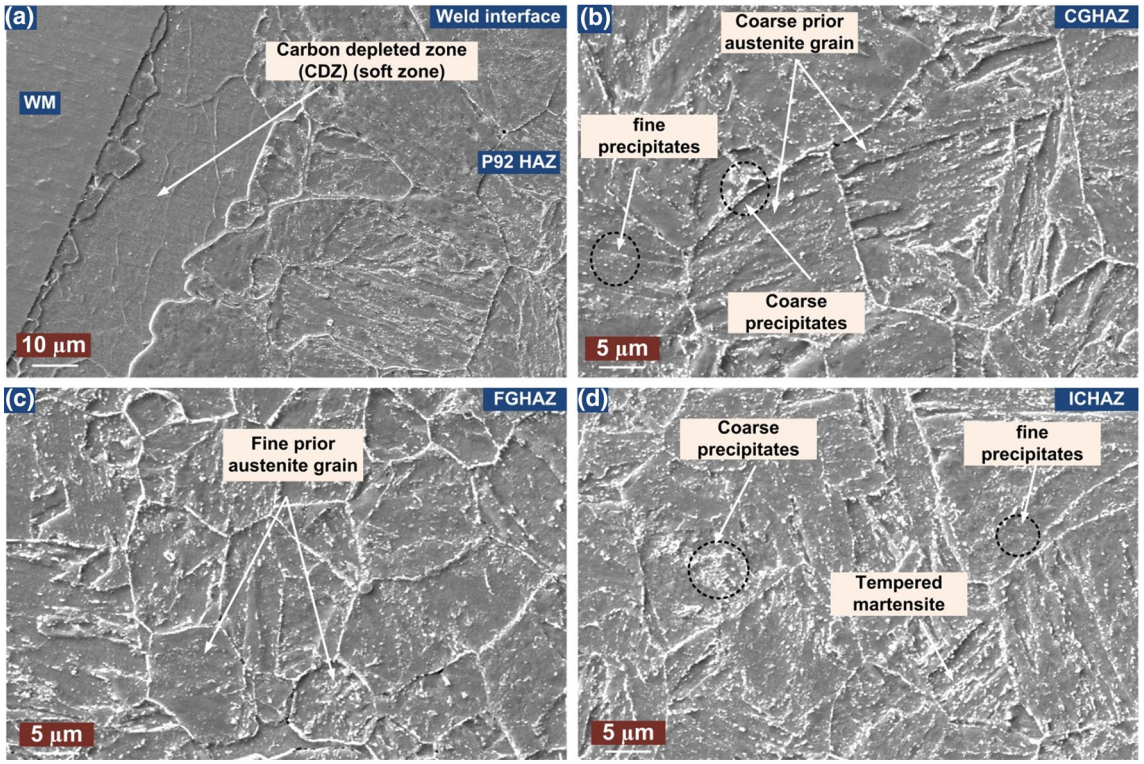

Fig. 23 After PWHT, SEM microstructure of **a** weld and P92HAZ interface **b** CGHAZ **c** FGHAZ and **d** ICHAZ for narrow groove design

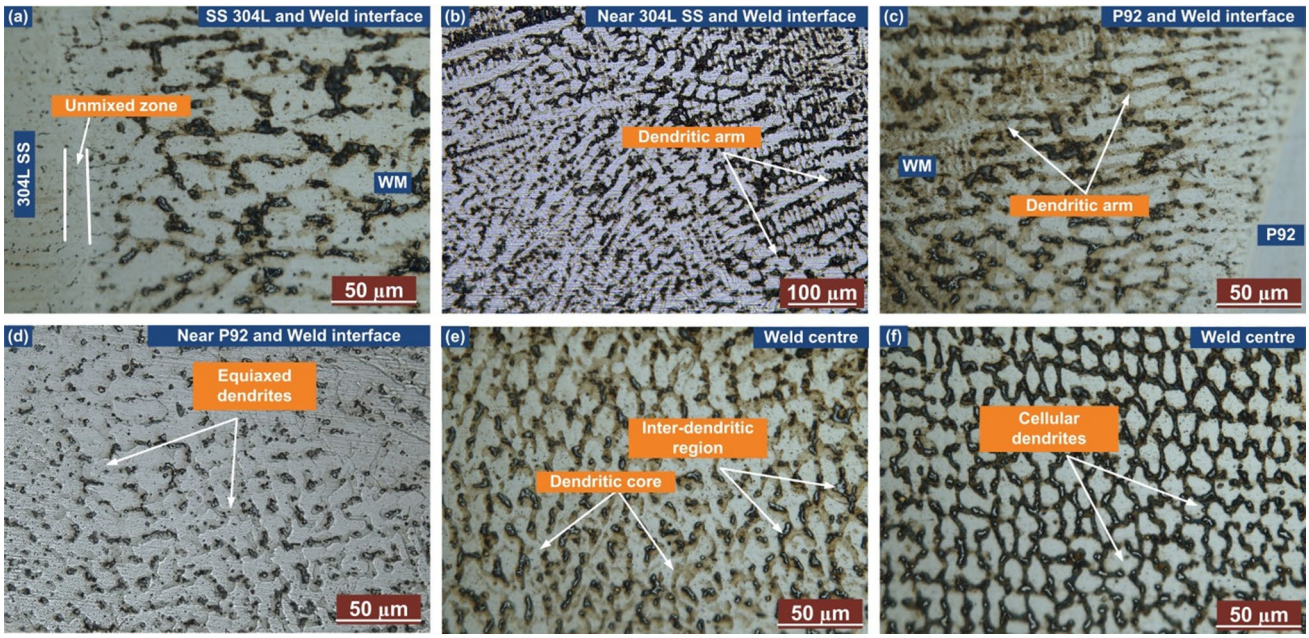

Fig. 24 After PWHT, optical microstructure of the ERNiFeCr-2 weld metal **a** 304L SS and weld interface **b** near 304L SS and weld interface **c** P92 and weld interface **d** near P92 and weld interface **e**, **f** weld center for V-groove design

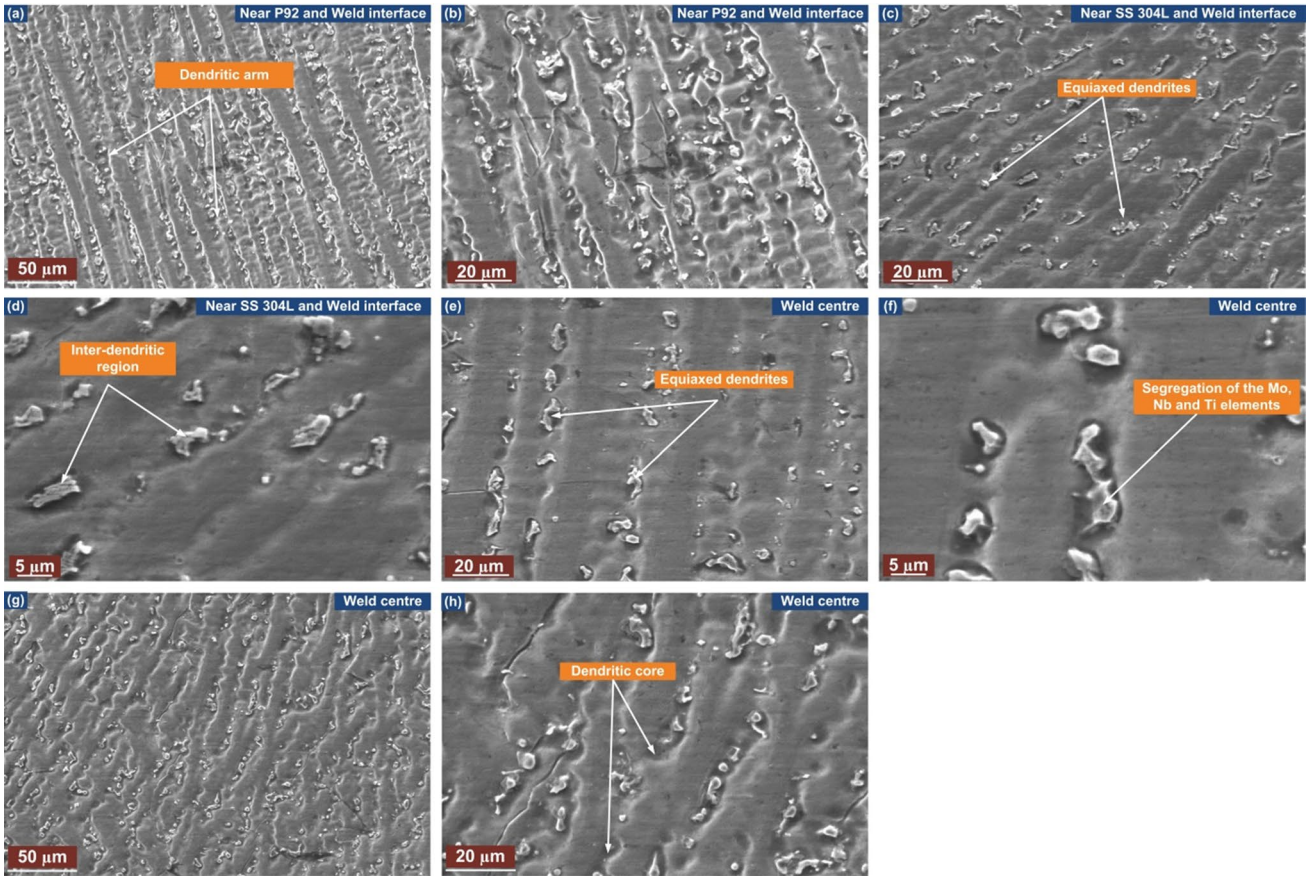

Fig. 25 After PWHT SEM microstructure of the ERNiFeCr-2 weld metal **a**, **b** near P92 and weld interface at low and high magnification **c**, **d** near 304L SS and weld interface at low and high magnification and **e–h** weld centre for V-groove design

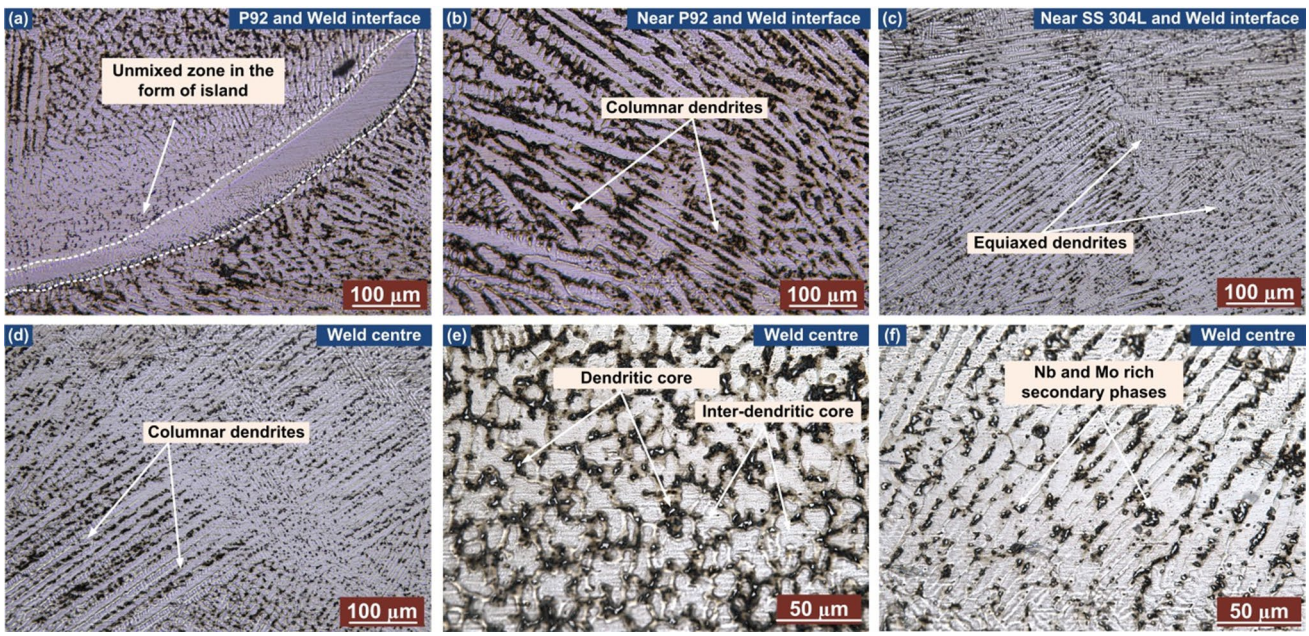

Fig. 26 After PWHT, optical microstructure of the ERNiFeCr-2 weld metal **a** P92 and weld interface **b** near P92 and weld interface **c** near 304L SS and weld interface **d–f** weld centre for narrow groove design

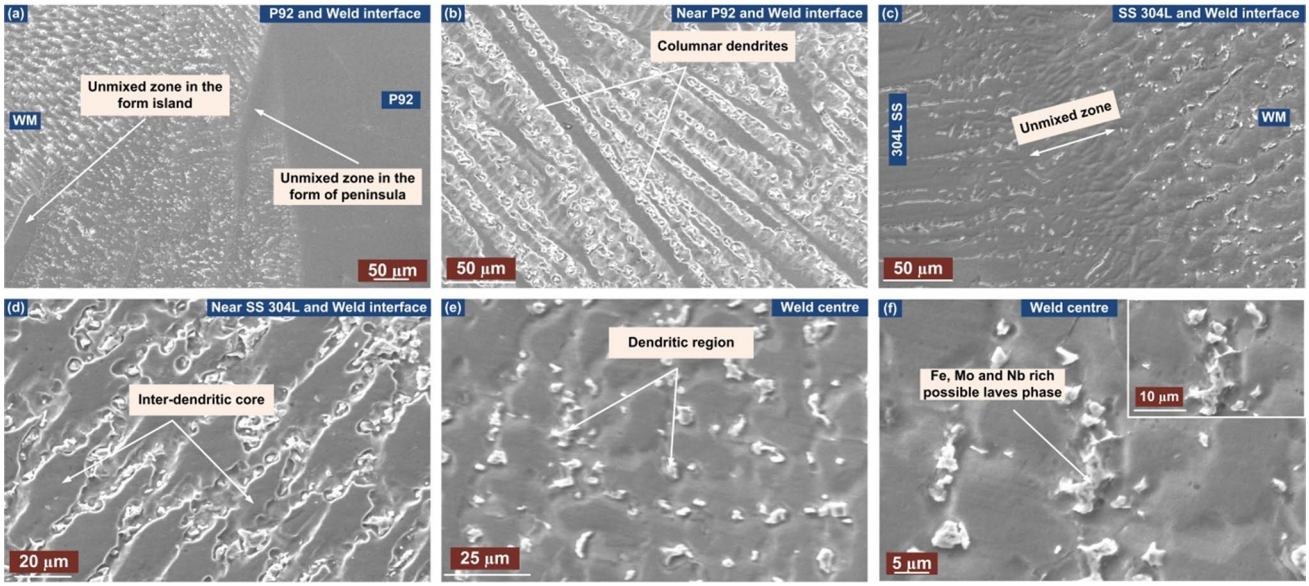

Fig. 27 After PWHT SEM microstructure of the ERNiFeCr-2 weld metal **a** P92 and weld interface **b** near P92 and weld interface **c** 304L SS and weld interface **d** near 304L SS and weld interface **e**, **f** weld centre for narrow groove design

of the P92-304L SS DWJs. The tensile properties of the P92/304L SS DWJs for V-shape groove design and narrow groove design in as-weld states and after PWHT are listed in Table 6. The mechanical properties of the base metals and P92/304L SS DWJs in as-weld and PWHT state are also given in Table 6. It was noticed from the fractured specimens of the V-groove DWJs that the weld fusion zone undergoes plastic deformation during loading, but failure took place from the weld and 304L interface for the as-welded specimen and the 304L BM for the PWHT specimen. An as-welded specimen did not present a necking phenomenon due to the plastic deformation, but the PWHT specimen presented a necking phenomenon. A brittle fracture was observed for the as-welded specimen, while a ductile fracture was observed for the PWHT specimen. It was observed from the fractured specimens of the narrow groove DWJs that the failure took place from the weld and 304L interface for both as-welded and PWHT specimens. It was also noticed from the fractured specimens of narrow groove DWJs that the weld fusion zone undergoes plastic deformation during loading, but necking was absent for these specimens. The strength value of both the as-weld

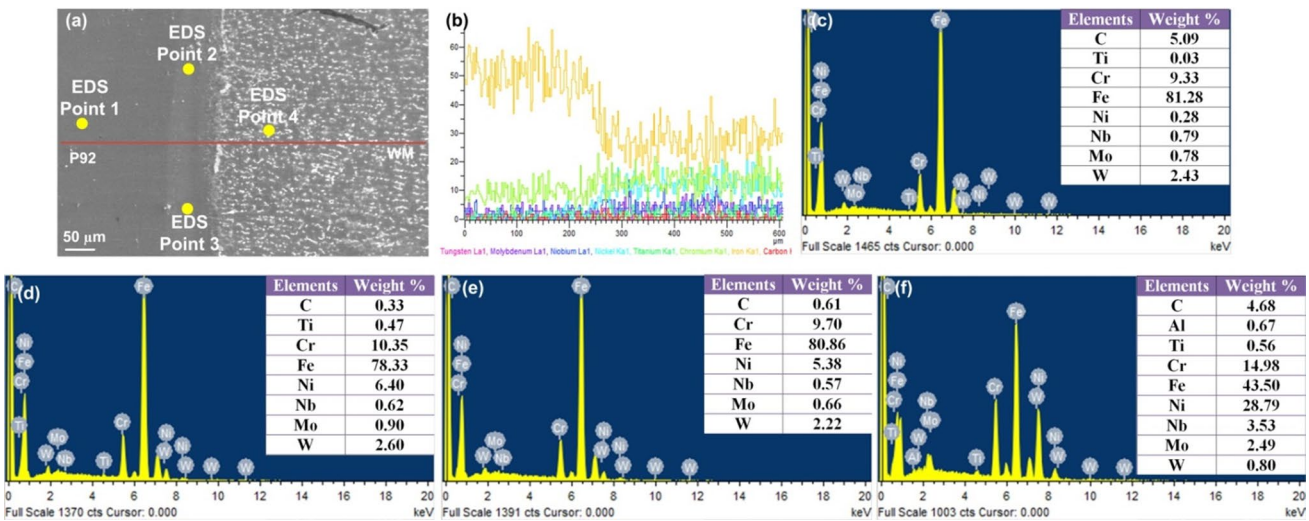

Fig. 28 **a** EDS analysis location across P92 and WM, **b** Line map across the P92 and WM, **c** EDS result of point 1, **d** EDS result of point 2, **e** EDS result of point 3, **f** EDS result of point 4

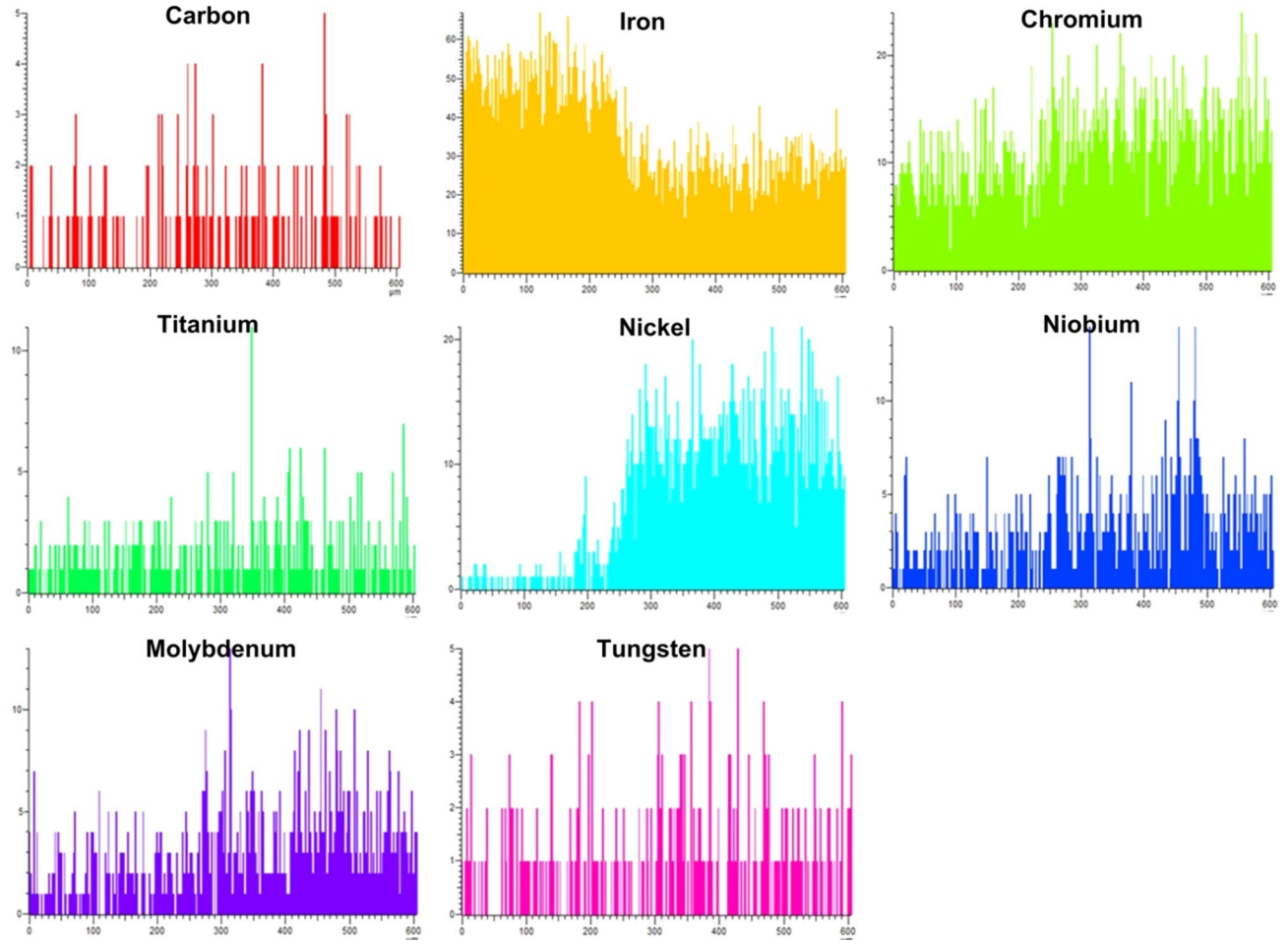

Fig. 29 Line mapping across the ERNiCrFe-2 weld metal and P92 base metal

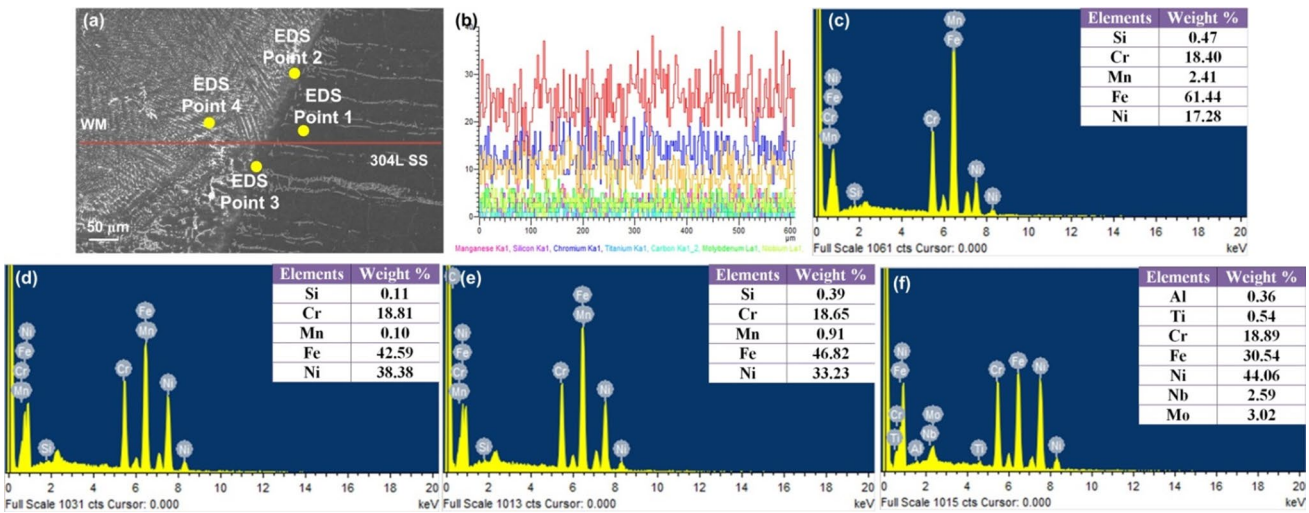

Fig. 30 **a** EDS analysis location across 304L SS and WM, **b** Line map across the 304L SS and WM, **c** EDS result of point 1, **d** EDS result of point 2, **e** EDS result of point 3, **f** EDS result of point 4

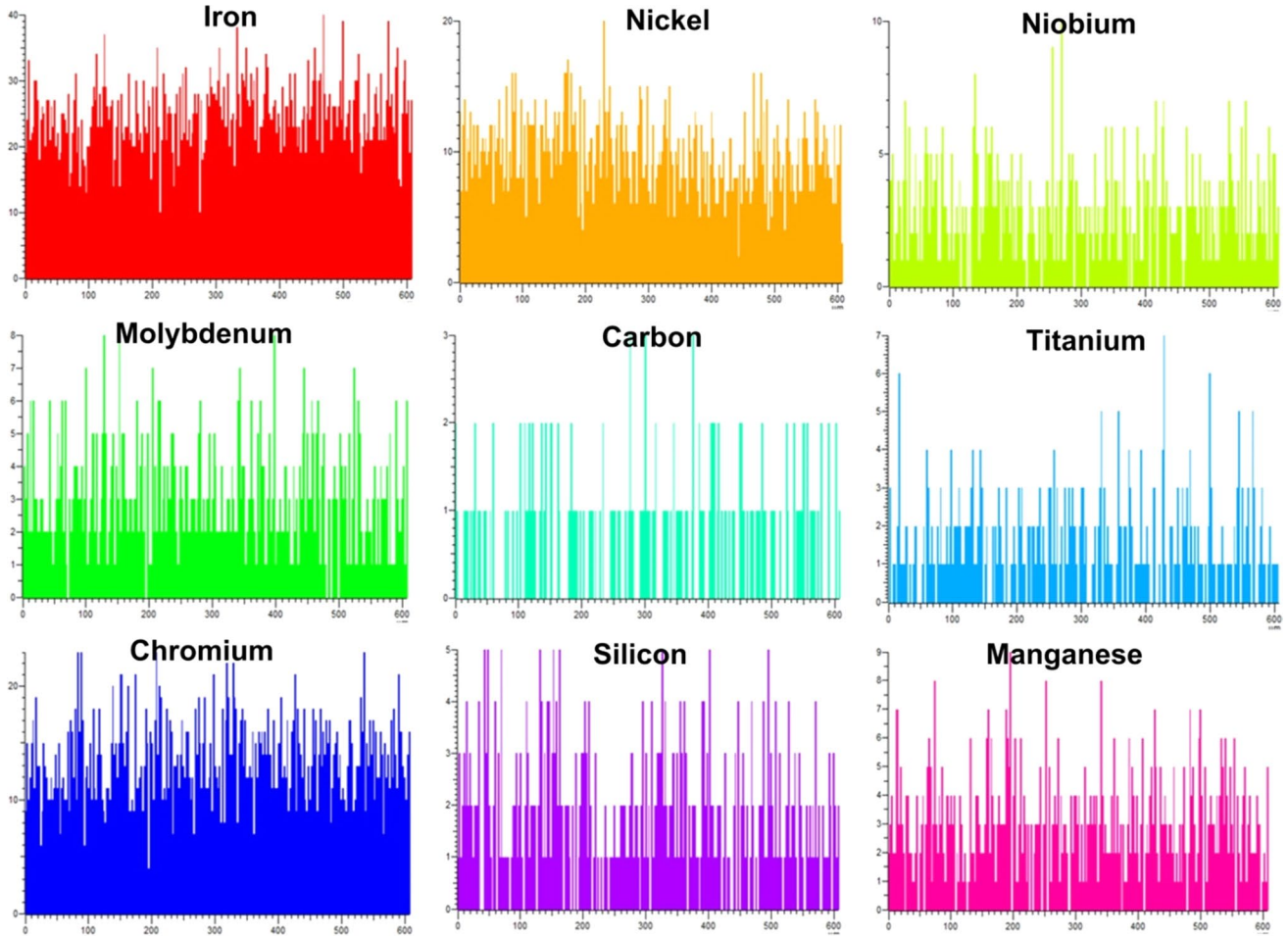

Fig. 31 Line mapping across the ERNiCrFe-2 weld metal and 304L SS base metal

and PWHT specimen was found to be the same, but the elongation and yield strength of the PWHT specimen was higher than the as-weld specimen due to the tempering of the martensite during the PWHT. The UTS value of the P92/304L SS DWJs in as-weld and PWHT state was almost equal to the UTS value of the 304L SS BM. The ultimate tensile strength (UTS) value for the V-groove profile as-weld and PWHT joint was measured as 630 and 621 MPa, respectively, which was closer to the 304L SS strength (632 MPa) but less than the UTS value of the P92 steel (758 MPa). The ultimate tensile strength (UTS) value for narrow groove profile as-weld and PWHT joint was measured as 620 and 629 MPa, respectively, which was again closer to the 304L SS strength (632 MPa). It means the tensile strength of the weld joint is similar to the 304L SS steel. Thus, the results obtained also confirm the accuracy of the tensile test. The tensile test result indicates that P92/304L SS DWJ has sufficient weld strength to qualify for the USC boiler requirement. The tensile test acceptance criteria according to the ASME BPVC Section IX are as follows: "If the specimen breaks in the base metal outside of the weld or weld interface, the test shall be accepted as meeting the requirements, provided the strength is not more than 5% below the minimum specified tensile strength of the base metal". Thus, according to this criterion also, specimens were qualified in the tensile test. Also, it should be noted that the ductility or percentage elongation of the P92/304L SS DWJ in as-weld and PWHT state was different from the 304L SS BM. The tensile test results also support the result of the hardness test. The failure occurred from the 304L BM owing to its low hardness value.

3.5 V-notch impact toughness

The Charpy V-notch impact test was performed on P92/304L DWJs specimens in as-weld and after PWHT. The results of the Charpy impact test carried out on V-shape and narrow shape groove geometry specimens have been shown in bar chart form, as shown in Fig. 36a, b. The V-notch was created

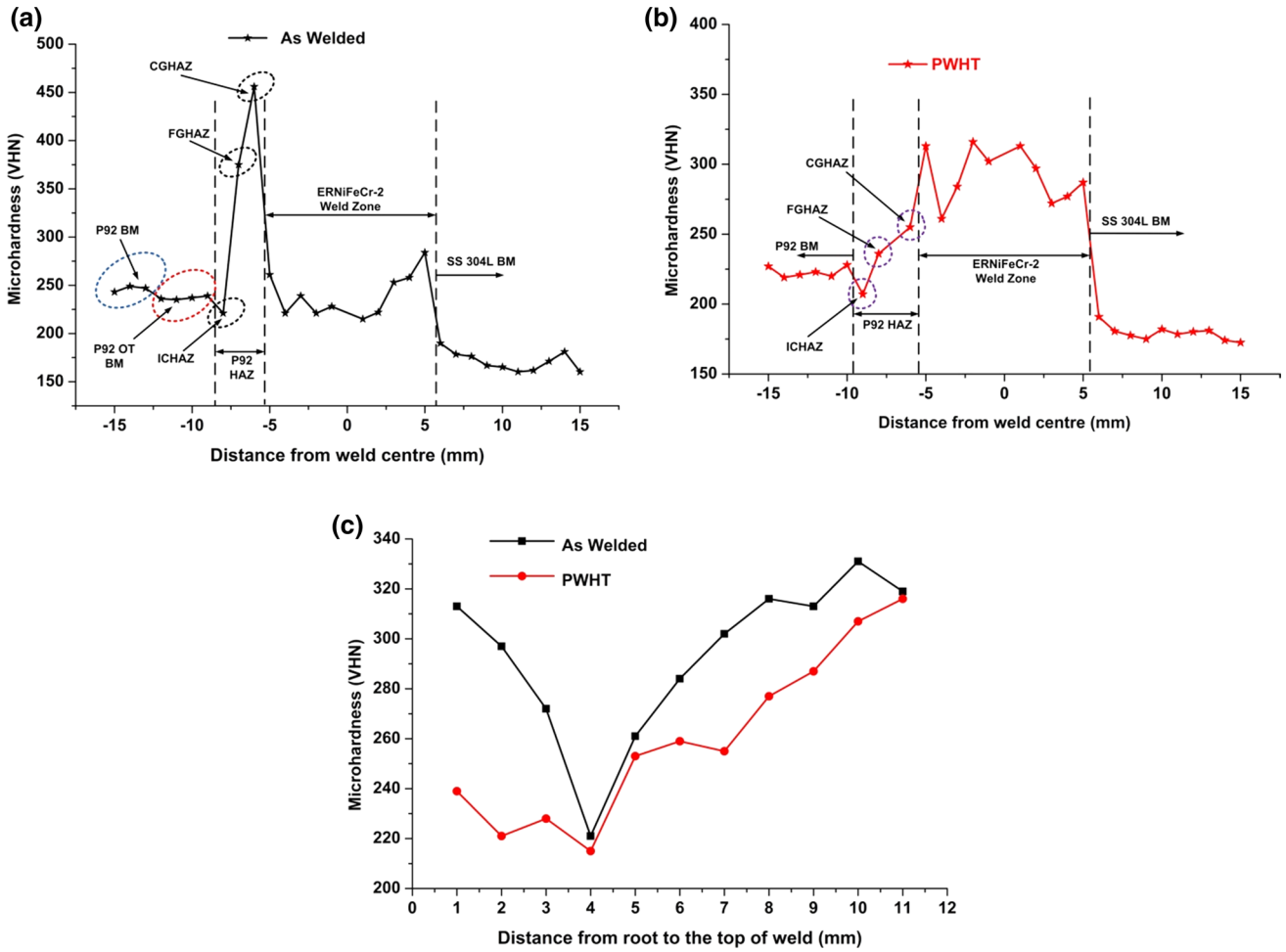

Fig. 32 For V-shape groove profile micro-hardness distribution across P92-ERNiFeCr-2-304L SS DWJ **a** As-weld state, **b** After PWHT and **c** from root to the top of ERNiFeCr-2 weld fusion zone in as-weld state and after PWHT

at the ERNiFeCR-2 weld zone, P92 HAZ, and 304L SS HAZ (inset image in Fig. 36a, b). The V-notch impact toughness of the ERNiFeCr-2 filler weld metal for V-groove geometry welded DWJs was 33 and 25 J in the as-weld state and after PWHT, respectively. The impact toughness result observed for ERNiFeCr-2 weld fusion zone for narrow groove geometry welded DWJs was 35 and 28 J in as-weld and PWHT conditions, respectively, lower than P92 and 304L BM. It can be concluded that the impact energy of the ERNiFeCr-2 filler weldments is much lower than the nickel-based filler like ERNiCrMo-3 (48 J), ERNiCrMoCo-1 (55 J), and ERNiCr-3 (58 J) in as-weld condition [48–50]. The Charpy test result showed the brittle fracture of the weld metal as specimens fractured in two halves. The drastic reduction in the impact toughness of the weld metal may be due to the formation of the Nb and Mo-rich secondary phases. The formation of secondary phases in the inter-dendritic region deteriorates the toughness and ductility. The crack initiation is also facilitated through the Nb-rich secondary phases in the inter-dendritic region. This results in the low toughness of the weld [17]. Also, the presence of a high amount of the Fe in the ERNiFeCr-2 filler promotes the formation of the Nb-rich secondary phases in the weld metal. The presence of the Fe elements decreases the solubility of the Nb elements in the austenitic matrix, and thus more amounts of the Nb-rich secondary phases precipitate in the inter-dendritic regions. Thus, it is recommended to use low Fe and high Ni content filler metals [51, 52]. The ERNiFeCr-2 weld metal acts in a brittle manner in both as-weld and after PWHT state. According to the European standard EN 1599:1997, the minimum required impact energy to qualify for the USC application and minimize the risk of brittle fracture in the weld metal is 47 J (minimum single value of 38 J). The impact energy value for the ERNiFeCr-2 weld metal in as-weld and PWHT state was below the minimum impact energy requirement. The P92 HAZ region impact toughness was observed as 145 J in as-weld condition. The low toughness value of the P92 HAZ region after welding was due to

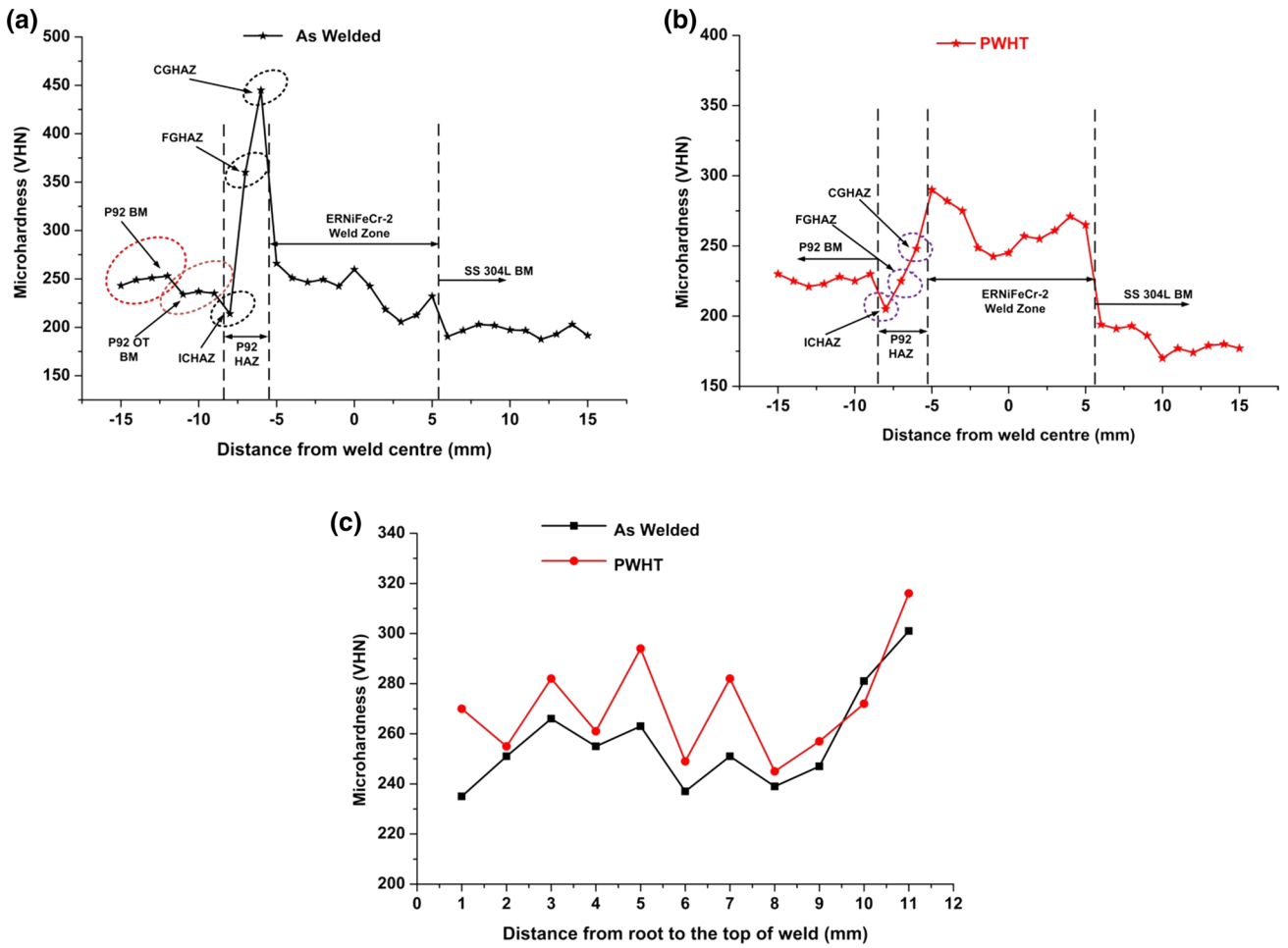

Fig. 33 For narrow groove profile micro-hardness distribution across P92- ERNiFeCr-2-304L SS DWJ **a** In as-weld state, **b** After PWHT and **c** from root to the top of ERNiFeCr-2 weld fusion zone in as-weld state and after PWHT

the dissolution of the precipitates and formation of the brittle quenched lath martensite microstructure, as discussed in previous sections. After PWHT, toughness reaches 170 J. The PWHT increases the toughness of the P92 HAZ due to the tempering of the quenched lath martensitic structure and the evolution of the precipitates. The impact toughness of 304L SS HAZ was 265 and 255 J in as-weld and PWHT situations, respectively. The welding does not significantly affect the toughness property of the 304L SS. The toughness value was very close to the strength of the 304L SS BM. Also after PWHT, toughness was the same as before the PWHT process. Thus, it can be said that the welding and PWHT have no significant effect on the mechanical and microstructural properties of 304L SS metal.

Table 5 Micro-hardness value (HV0.5) of the HAZ region

	V-groove profile		Narrow groove profile	
	As-weld	PWHT	As-weld	PWHT
CGHAZ	456	255	445	248
FGHAZ	375	236	360	225
ICHAZ	221	207	214	205

3.6 Residual stress measurements

Figures 37a–c and 38a–c show the longitudinal and transverse residual stress distribution for V-shape and narrow shape groove profile, respectively. The through-thickness longitudinal and transverse residual stress distribution in the as-weld state and after PWHT for the weld metal, P92 HAZ, and 304L SS HAZ is presented in Figs. 37a–c and 38a–c. For the ERNiFeCr-2 filler weld metal, tensile longitudinal and transverse residual stresses were present in as-weld and PWHT situation. The tensile residual stresses were developed because of the volumetric solidification of the weld metal during the solidification. The volume shrinkage effect due to the weld solidification and volumetric expansion due to the martensitic transformation of the weld are the key factors that govern the nature of the welding induce

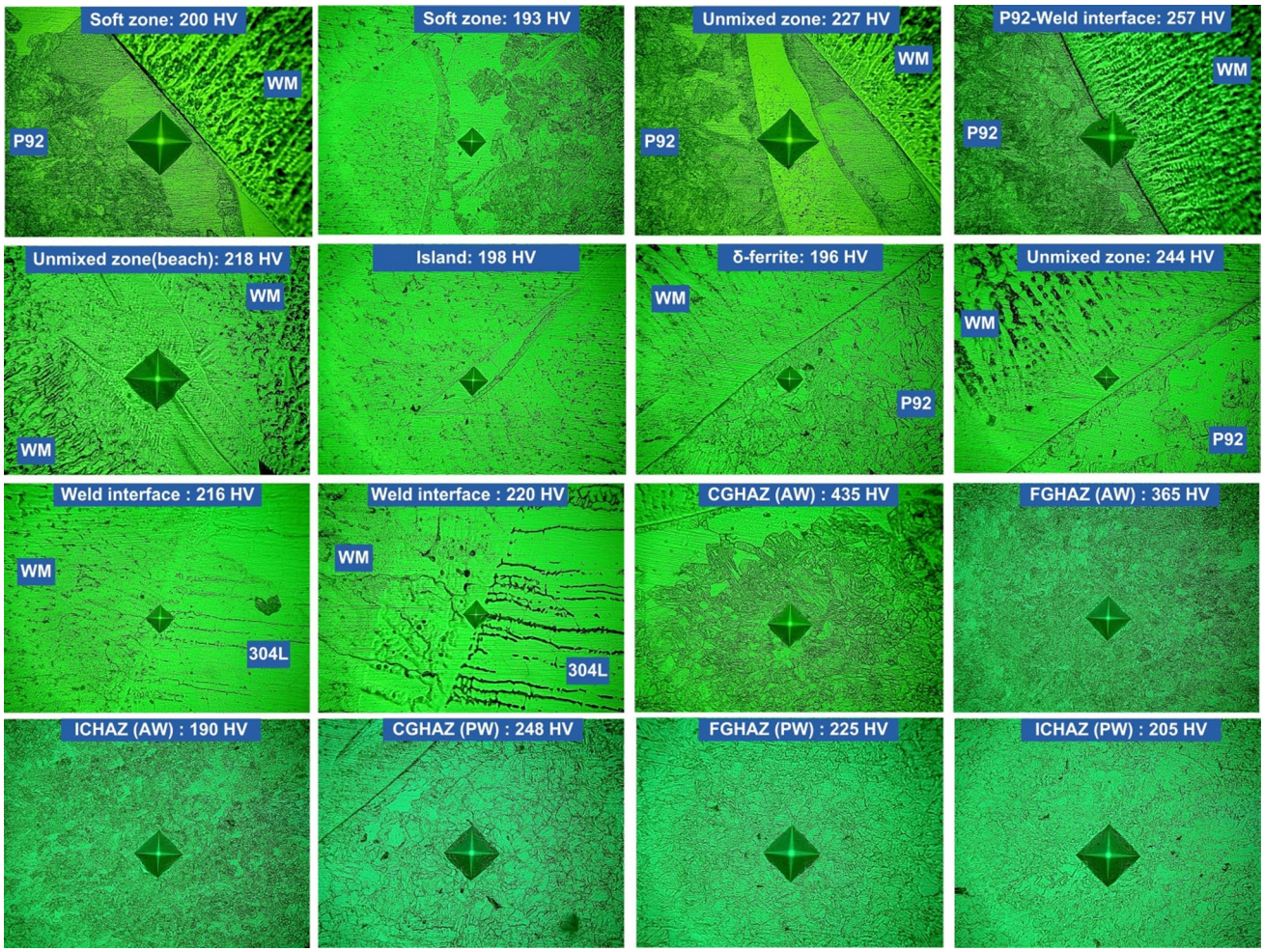

Fig. 34 Micro-hardness value at critical locations across P92/304L SS DWJs

residual stresses. The volume shrinkage effect due to the weld solidification induces the tensile residual stresses, while the volumetric expansion due to the martensitic transformation induces the compressive residual stresses [19]. In the present case, nickel-based filler metal was used. Thus volumetric shrinkage effect due to the weld solidification was more dominant. This induces the tensile residual stresses in the weld metal. After PWHT also, the tensile residual stresses were observed in the weld fusion zone. The significant difference in the coefficient of thermal expansion value between ferritic and austenitic steel develops the high tensile residual stresses at the weld interface (approximately the yield strength of the material). For the ERNiFeCr-2 filler weld fusion zone of the V shape groove profile, the maximum longitudinal tensile residual stress of 377 MPa was observed at the top surface of the weld. The tensile residual stress was reduced at the root pass because of the tempering effect from the subsequent passes. For the ERNiFeCr-2 filler weld fusion zone of narrow shape groove profile, the maximum longitudinal compressive residual stress of 304 MPa was observed at the top surface of the weld. After PWHT for the ERNiFeCr-2 filler weld fusion zone of the V shape groove profile, the maximum longitudinal tensile residual stress of 192 MPa was observed at the top surface of the weld. After PWHT for the ERNiFeCr-2 filler weld fusion zone of narrow shape groove profile, the maximum longitudinal tensile residual stress of 187 MPa was observed at the top surface of the weld. Similar kinds of trends were observed for the transverse residual stresses. Thus, it can be concluded that PWHT and narrow groove geometry minimize the welding-induced residual stresses. Also, the residual stress distribution shows that the welding-induced residual stresses were maximum between the top surfaces of the weld up to the depth of 5 mm. From the center (after the depth of 5 mm) to the bottom of the weld, residual stresses were gradually decreased.

Also, for the P92 HAZ and 304L HAZ, the longitudinal and transverse residual stresses for the narrow groove geometry were lesser than that for the V shape groove geometry in the as-weld state and after PWHT. For P92 HAZ,

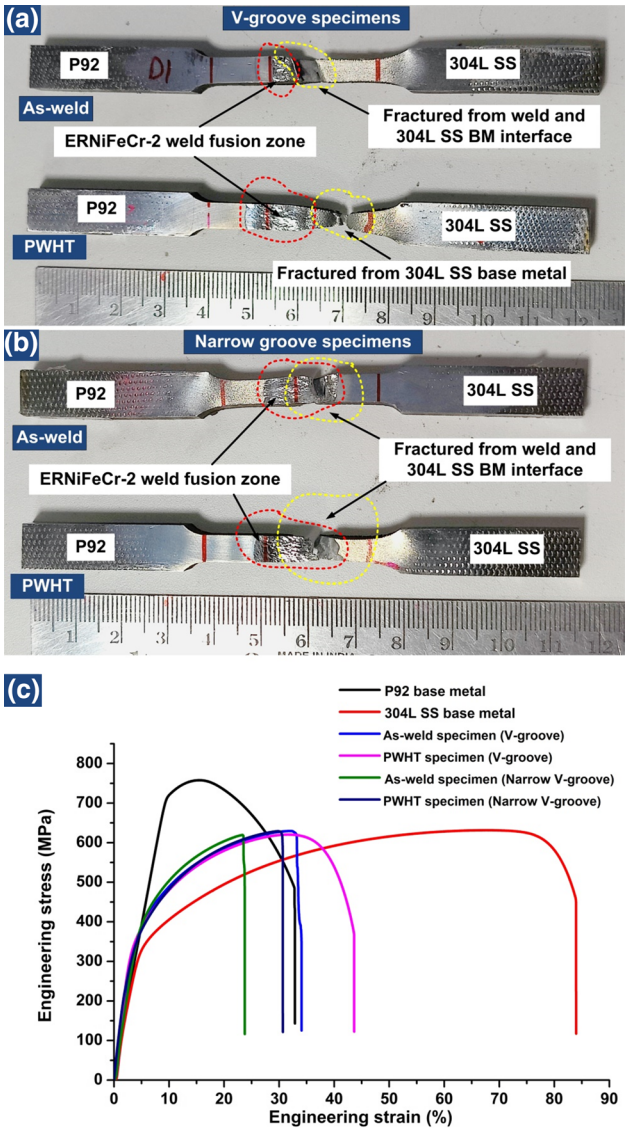

Fig. 35 **a**, **b** Tensile specimens after fracture and **c** stress–strain curve

compressive residual stresses were observed because of the volumetric expansion due to the martensitic transformation. When P92 steel is heated above Ac_1 temperature, its body-centered cubic (BCC) structure transforms into a face-centered cubic (FCC) structure, during this volume decreases. When it is cooled, its FCC structure transforms into a body-centered tetragonal (BCT) structure, during this volume increases. This volumetric change causes the yield strength changes. These yield strength changes cause a change in residual stress magnitude and alter the sign of residual stresses [53]. For 304L SS HAZ, tensile residual stresses were observed in as-weld and after PWHT. The high tensile residual stresses are developed in 304L SS due to its low thermal conductivity and a high coefficient of thermal expansion. Because of the absence of the phase transformation in the 304L SS, the residual stresses were observed to be very much of the same nature. The high tensile residual stresses in the austenitic stainless steel may be due to its high thermal expansion value. The mismatch in the coefficient of the thermal expansion between the P92 steel and 304L SS results in the variation of the residual stress across weld fusion zone, P92 HAZ, and 304L SS HAZ. The high tensile residual stress in the 304L HAZ and ERNiFeCr-2 weld metal indicates its high susceptibility to cracking [54]. From the residual stress analysis for both the V-shape and narrow shape groove geometry, it can be stated that welding-induced residual stresses for the narrow shape groove geometry were lower than those of the V-shape groove geometry. This may be due to the less weld metal deposition for the narrow groove design as compared to the V-shape groove geometry. This results in less shrinkage of the weld metal and thus less residual stresses than the V-shape groove profile [26]. Li et al. [55] investigated the residual stresses for P92/SUS 304 dissimilar metal butt weld joints with single V-groove and X-groove geometry. They concluded that X-groove geometry is superior compared to the single V-groove design in reducing tensile residual stresses. The authors also reported that martensitic phase transformation in P92 steel, strain hardening in the SUS 304 steel, and discrepancy in the coefficient of thermal expansion are the key

Table 6 Mechanical properties of the base metal and P92/304L SS DWJs

DWJ condition	Tensile strength (MPa)	0.2% yield strength	% elongation	Fracture location	Joint efficiency (%)
P92 BM	758	710	32.87	–	–
304L SS BM	632	209	83.96	–	–
V-groove design					
As-welded	630	228	34.08	Weld and 304L interface	99.68
PWHT	621	273	43.63	304L BM	98.26
Narrow groove design					
As-welded	620	335	23.75	Weld and 304L interface	98.10
PWHT	629	237	30.66	Weld and P92 interface	99.52

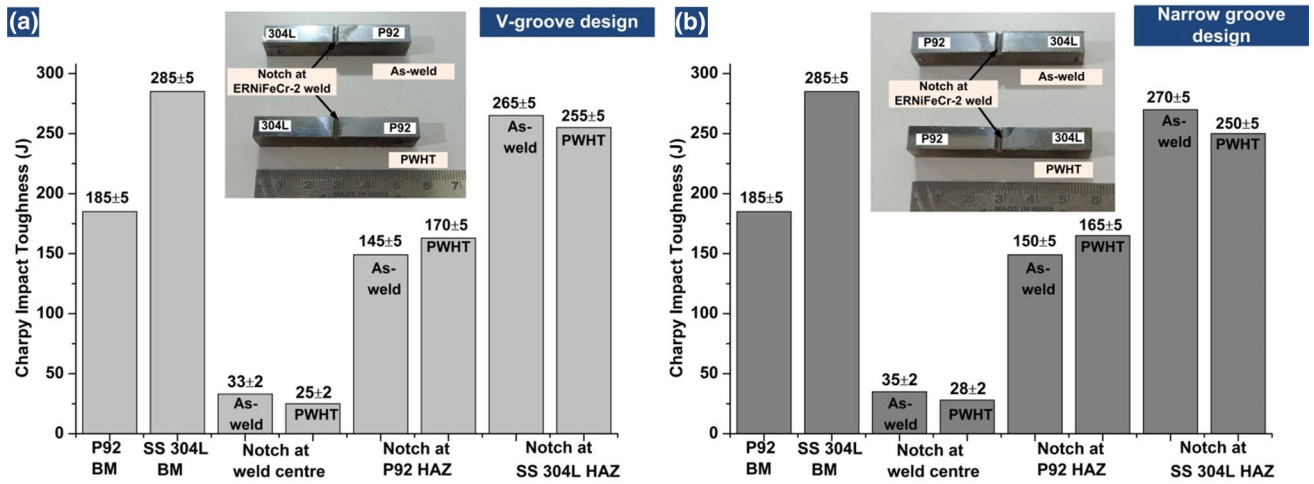

Fig. 36 Charpy impact toughness (J) at the RT **a** for V-groove design and **b** for narrow groove design

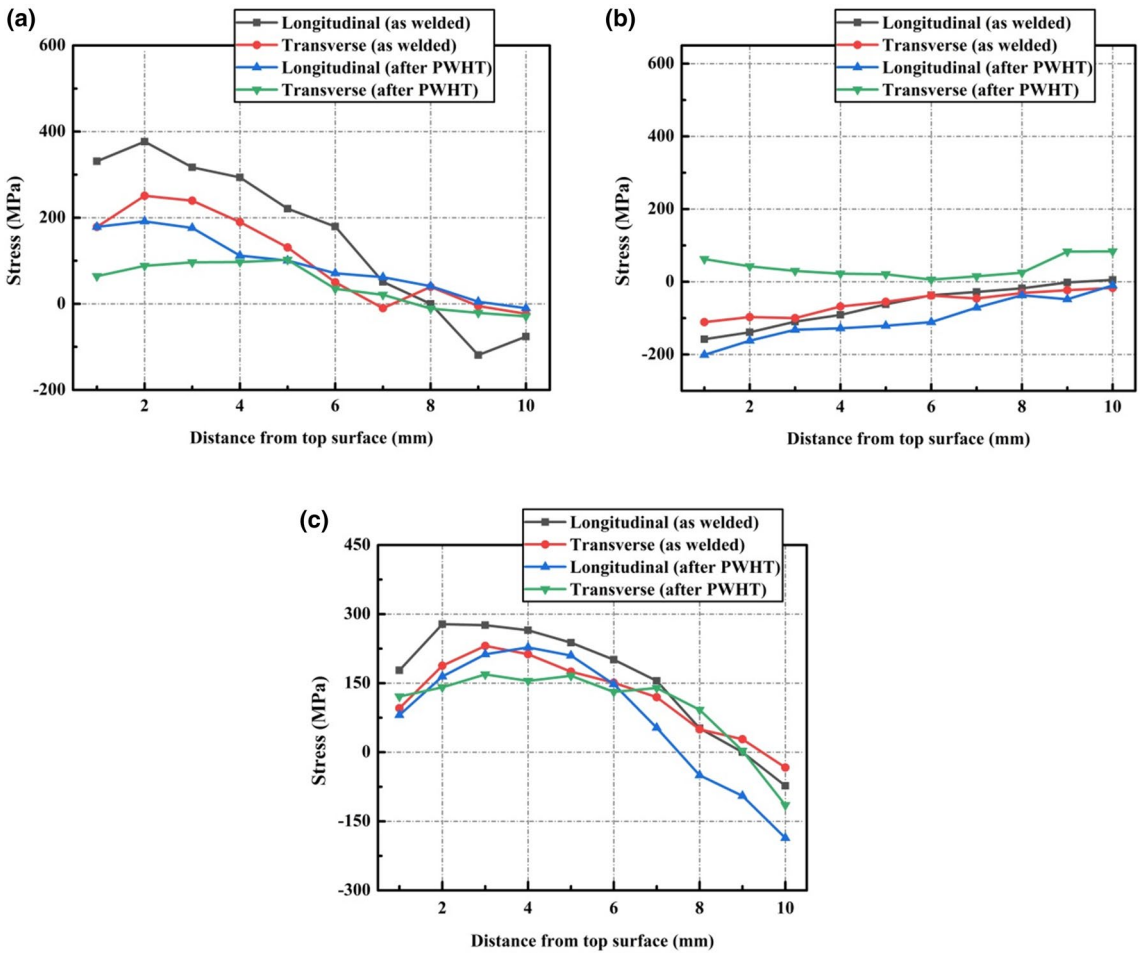

Fig. 37 Distribution of welding induced residual stresses in as-weld and PWHT condition for **a** weld metal, **b** P92 HAZ, and **c** 304L SS HAZ for V-shape groove profile

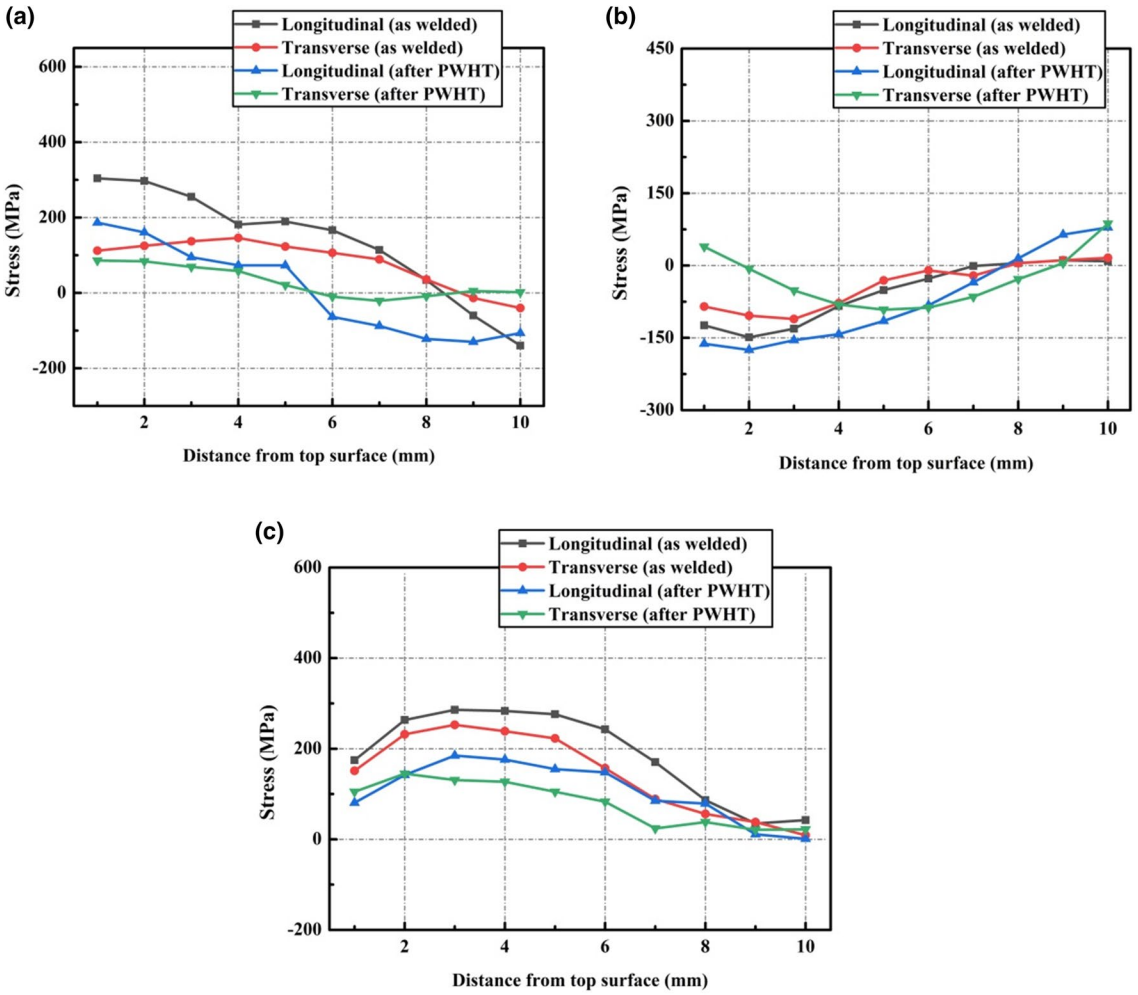

Fig. 38 Distribution of weld-induced residual stresses in as-weld and PWHT conditions for **a** weld metal, **b** P92 HAZ, and **c** 304L SS HAZ for narrow shape groove profile

factors influencing the residual stress variation. Zhao et al. [56] performed the numerical simulation of residual stresses for P92/304H dissimilar metal butt weld joints with single V-groove geometry of varying groove angles. They concluded that a small groove angle with more welding passes decreases the residual stresses.

4 Conclusions

From the analysis and comparison of the microstructure characteristics, mechanical properties, and residual stresses in as-weld and PWHT state for two different groove profiles, the key findings can be summarized as follows:

(1) From the comparison of the V-groove and narrow groove profile, it was found that the narrow groove design requires less filler metal than the conventional V-groove design. Also, a narrow groove design significantly reduces HAZ width and HAZ area due to less heat input. The overall time required to complete the welding was also less for narrow groove design DWJs.

(2) The microstructure analysis showed the existence of the unmixed zone in the form of the beach, peninsula, and island at the interface of the base metal and weld metal. The formation of the soft ferrite zone at P92 HAZ and ferrite stringers at SS 304L HAZ was observed. The Mo, Nb, and Ti–rich precipitates were observed at the weld fusion zone.

(3) The average coarse grain size in the case of the narrow groove design was found to be lower than the conventional groove design. This may be due to the less heat input and low peak temperature experienced by the CGHAZ during the welding for the narrow groove design.

(4) The fracture specimens revealed that the weld interface is the weakest region in P92-ERNiFeCr-2-304L SS DWJs as the failure occurred from the weld interface in most cases. However, the tensile strength value of these DWJs was very close to the minimum tensile strength value between the two base metals (304L SS). As in the majority of the cases, the specimen was failed from the weld interface, it can be inferred that ERNiFeCr-2 filler metal is less compatible with the 304L SS and P92 metal due to the more segregation of the Mo and Nb elements.

(5) The micro-hardness profile shows an increasing trend from the weld fusion zone towards the P92 HAZ in the as-weld situation. The hardness profile was stable from the weld fusion zone toward the 304L SS HAZ, and 304L SS BM. Micro-hardness test showed that SS 304L base metal has a low hardness value compared to the other region. This was confirmed by the tensile test result, as the specimens failed from the weld and SS 304 L base metal interface. After PWHT, the hardness of the weld fusion zone was increased due to the precipitation hardening effect.

(6) The impact toughness of the ERNiFeCr-2 filler weld was below the minimum requirement of 47 J. The ERNiFeCr-2 weld fusion zone has a low toughness value of 33 J (AW) and 25 J (PWHT) for V-groove design and 35 J (AW) and 28 J (PWHT) for narrow groove design. The low toughness value was due to the formation of the secondary phases and solidification segregation.

(7) From the residual stress profile for both V-shape and narrow shape groove geometry, it can be concluded that longitudinal and transverse residual stress of tensile nature was observed for ERNiFeCr-2 weld metal. However, longitudinal and transverse residual stress of compressive nature was observed at the root pass. From the residual stress distribution for weld metal, it can be stated that maximum longitudinal and transverse residual stresses were developed at the top surface of weld metal. It was observed that PWHT resulted in the significant minimization of the residual stresses of the weld metal. However, the nature of residual stresses was the same before and after PWHT.

Acknowledgements The authors sincerely acknowledge the financial support for this research work provided by the "Science and Engineering Research Board" (SERB-India) under the grant No: SRG/2019/001879 for the project entitled "Mitigation of weldability issues and residual stresses in dissimilar welded joints of ultra-supercritical power plants".

Declarations

Conflict of interest No conflict of interest.

Research involving human participants and/or animals This article does not contain any studies with animals performed by any of the authors.

References

1. Pandey C, Mahapatra MM, Kumar P. Effect of post weld heat treatments on fracture frontier and type IV cracking nature of the crept P91 welded sample. Mater Sci Eng A. 2018;731:249–65. https://doi.org/10.1016/j.msea.2018.06.038.
2. Dak G, Pandey C. A critical review on dissimilar welds joint between martensitic and austenitic steel for power plant application. J Manuf Process. 2020;58:377–406. https://doi.org/10.1016/j.jmapro.2020.08.019.
3. Siefert JA, David SA, Siefert JA, David SA. Weldability and weld performance of candidate austenitic alloys for advanced ultrasupercritical fossil power plants Weldability and weld performance of candidate austenitic alloys for advanced ultrasupercritical fossil power plants. Sci Technol Weld Join. 2014;19:271–94.
4. Li T, Yuan X, Li R, Xiong J, Tao S, Wu K. Microstructure and mechanical characteristics of dissimilar TIG welded 9% Cr heat-resistant steels joints. Int J Precis Eng Manuf. 2021;22:1007–19. https://doi.org/10.1007/s12541-021-00517-x.
5. Kumar A, Pandey C. Autogenous laser-welded dissimilar joint of ferritic/martensitic P92 steel and Inconel 617 alloy: mechanism, microstructure, and mechanical properties. Arch Civ Mech Eng. 2022;22:39. https://doi.org/10.1007/s43452-021-00365-6.
6. Wang HT, Wang GZ, Xuan FZ, Tu ST. Fracture mechanism of a dissimilar metal welded joint in nuclear power plant. Eng Fail Anal. 2013;28:134–48. https://doi.org/10.1016/j.engfailanal.2012.10.005.
7. Kepic J, Falat L, Lucia C. Correlation between microstructure and creep performance of martensitic / austenitic transition weldment in dependence of its post-weld heat treatment. Eng Fail Anal. 2014;40:141–52. https://doi.org/10.1016/j.engfailanal.2014.02.018.
8. Kim M, Kwak S, Choi I, Lee Y, Suh J, Fleury E, Jung W, Son T. Materials Characterization High-temperature tensile and creep deformation of cross-weld specimens of weld joint between T92 martensitic and Super304H austenitic steels. Mater Charact. 2014;97:161–8. https://doi.org/10.1016/j.matchar.2014.09.011.
9. Karthick K, Malarvizhi S, Balasubramanian V, Gourav Rao A. Tensile properties variation across the dissimilar metal weld joint between modified 9Cr–1Mo ferritic steel and 316LN stainless steel at RT and 550 °C. Metallogr Microstruct Anal. 2018;7:209–21. https://doi.org/10.1007/s13632-018-0430-9.
10. Sirohi S, Gupta A, Pandey C, Vidyarthy RS, Guguloth K, Natu H. Investigation of the microstructure and mechanical properties of the laser welded joint of P22 and P91 steel. Opt Laser Technol. 2022;147: 107610. https://doi.org/10.1016/j.optlastec.2021.107610.
11. Falat L, Čiripová L, Kepič J, Buršík J, Podstranská I. Correlation between microstructure and creep performance of martensitic/austenitic transition weldment in dependence of its post-weld

heat treatment. Eng Fail Anal. 2014;40:141–52. https://doi.org/10.1016/j.engfailanal.2014.02.018.
12. Sun Z. Feasibility of producing ferritic/austenitic dissimilar metal joints by high energy density laser beam process. Int J Press Vessel Pip. 1996;68:153–60. https://doi.org/10.1016/0308-0161(94)00048-4.
13. DuPont JN, Kusko CS. Technical note: Martensite formation in austenitic/ferritic dissimilar alloy welds. Weld. J. (Miami, Fla). 86; 2007.
14. Mortezaie A, Shamanian M. An assessment of microstructure, mechanical properties and corrosion resistance of dissimilar welds between Inconel 718 and 310S austenitic stainless steel. Int J Press Vessel Pip. 2014;116:37–46. https://doi.org/10.1016/j.ijpvp.2014.01.002.
15. Ye X, Hua X, Wang M, Lou S. Controlling hot cracking in Ni-based Inconel-718 superalloy cast sheets during tungsten inert gas welding. J Mater Process Technol. 2015;222:381–90. https://doi.org/10.1016/j.jmatprotec.2015.03.031.
16. Mishra D, Vignesh MK, Raj BG, Srungavarapu P, Devendranath Ramkumar K, Arivazhagan N, Narayanan S. Mechanical characterization of Monel 400 and 316 stainless steel weldments. Procedia Eng. 2014;75:24–8.
17. Devendranath Ramkumar K, Sidharth D, Phani PP, Rajendran R, Giri Mugundan K, Narayanan S. Microstructure and properties of inconel 718 and AISI 416 laser welded joints. J Mater Process Technol. 2019;266:52–62.
18. Wang Y, Li L, Kannan R. Transition from Type IV to Type I cracking in heat-treated grade 91 steel weldments. Mater Sci Eng A. 2018;714:1–13. https://doi.org/10.1016/j.msea.2017.12.088.
19. Maduraimuthu V, Vasudevan M, Muthupandi V, Bhaduri AK. Effect of activated flux on the microstructure, mechanical properties, and residual stresses of modified 9Cr-1Mo steel weld joints. Metall Mater Trans B. 2012;43:123–32. https://doi.org/10.1007/s11663-011-9568-4.
20. Dak G, Joshi J, Yadav A, Chakraborty A, Khanna N. Autogenous welding of copper pipe using orbital TIG welding technique for application as high vacuum boundary parts of nuclear fusion devices. Int J Press Vessel Pip. 2020;188:104225. https://doi.org/10.1016/j.ijpvp.2020.104225.
21. Thakare JG, Pandey C, Gupta A, Taraphdar PK, Mahapatra MM. Role of the heterogeneity in microstructure on the mechanical performance of the Autogenous Gas Tungsten Arc (GTA) welded dissimilar joint of F / M P91 and SS304L steel. Fusion Eng Des. 2021;168: 112616. https://doi.org/10.1016/j.fusengdes.2021.112616.
22. Sakthivel T, Sasikala G, Dash MK, Syamala Rao P. Creep deformation and rupture behavior of P92 steel weld joint fabricated by NG-TIG welding process. J Mater Eng Perform. 2019;28:4364–78.
23. Kulkarni S, Rajamurugan G, Ghosh PK. Prominence of narrow groove on pulsed current GMA and SMA welding of thick wall austenitic stainless steel pipe. Trans Indian Inst Met. 2021;74:2297–312. https://doi.org/10.1007/s12666-021-02298-3.
24. Feng J, Guo W, Irvine N, Li L. Understanding and elimination of process defects in narrow gap multi-pass fiber laser welding of ferritic steel sheets of 30 mm thickness. Int J Adv Manuf Technol. 2017;88:1821–30. https://doi.org/10.1007/s00170-016-8929-1.
25. Nivas R, Singh PK, Das G, Das SK, Kumar S, Mahato B, Sivaprasad K, Ghosh M. A comparative study on microstructure and mechanical properties near interface for dissimilar materials during conventional V-groove and narrow gap welding. J Manuf Process. 2017;25:274–83. https://doi.org/10.1016/j.jmapro.2016.12.004.
26. Giri A, Mahapatra MM, Sharma K, Singh PK. A study on the effect of weld groove designs on residual stresses in SS 304LN thick multipass pipe welds. Int J Steel Struct. 2017;17:65–75. https://doi.org/10.1007/s13296-016-0118-4.
27. Pandey C, Kumar N, Sirohi S, Rajasekaran T, Kumar S, Kumar P. Study on the effect of the grain refinement on mechanical properties of the P92 welded joint. J Mater Eng Perform. 2022. https://doi.org/10.1007/s11665-021-06536-z.
28. Das Banik S, Kumar S, Singh PK, Bhattacharya S, Mahapatra MM. Distortion and residual stresses in thick plate weld joint of austenitic stainless steel: Experiments and analysis. J Mater Process Technol. 2021;289:116944.
29. Ren S, Li S, Wang Y, Deng D, Ma N. Predicting welding residual stress of a multi-pass P92 steel butt-welded joint with consideration of phase transformation and tempering effect. J Mater Eng Perform. 2019;28:7452–63. https://doi.org/10.1007/s11665-019-04470-9.
30. Taraphdar PK, Mahapatra MM, Pradhan AK, Singh PK, Sharma K, Kumar S. Effects of groove configuration and buttering layer on the through-thickness residual stress distribution in dissimilar welds. Int J Press Vessel Pip. 2021;192: 104392. https://doi.org/10.1016/j.ijpvp.2021.104392.
31. Shin KY, Lee JW, Han JM, Lee KW, Kong BO, Hong HU. Transition of creep damage region in dissimilar welds between Inconel 740H Ni-based superalloy and P92 ferritic/martensitic steel. Mater Charact. 2018;139:144–52. https://doi.org/10.1016/j.matchar.2018.02.039.
32. David SA, Siefert JA, Feng Z. Welding and weldability of candidate ferritic alloys for future advanced ultrasupercritical fossil power plants. Sci Technol Weld Join. 2013;18:631–51. https://doi.org/10.1179/1362171813Y.0000000152.
33. Shakil M, Ahmad M, Tariq NH, Hasan BA, Akhter JI, Ahmed E, Mehmood M, Choudhry MA, Iqbal M. Microstructure and hardness studies of electron beam welded Inconel 625 and stainless steel 304L. Vacuum. 2014;110:121–6. https://doi.org/10.1016/j.vacuum.2014.08.016.
34. Kou S. Welding metallurgy. New York: Wiley; 2002.
35. Dev S, Ramkumar KD, Arivazhagan N, Rajendran R. Effect of continuous and pulsed current GTA welding on the performance of dissimilar welds involving aerospace grade alloys. Trans Indian Inst Met. 2017;70:729–39. https://doi.org/10.1007/s12666-017-1085-y.
36. Silva CC, De Miranda HC, Motta MF, Farias JP, Afonso CRM, Ramirez AJ. New insight on the solidification path of an alloy 625 weld overlay. J Mater Res Technol. 2013;2:228–37. https://doi.org/10.1016/j.jmrt.2013.02.008.
37. Mageshkumar K, Kuppan P. Microstructural evolution and precipitation behavior in heat affected zone of Inconel 625 and AISI 904L dissimilar welds Microstructural evolution and precipitation behavior in heat affected zone of Inconel 625 and AISI 904L dissimilar welds. IOP Conf Series Mater Sci Eng. 2017;263(6):062073. https://doi.org/10.1088/1757-899X/263/6/062073.
38. Kangazian J, Shamanian M, Ashrafi A. Dissimilar welding between SAF 2507 stainless steel and Incoloy 825 Ni-based alloy: The role of microstructure on corrosion behavior of the weld metals. J Manuf Process. 2017;29:376–88. https://doi.org/10.1016/j.jmapro.2017.08.012.
39. DuPont JN, Lippold JC, Kiser SD. Welding metallurgy and weldability of nickel-base alloys. Hoboken: Wiley; 2009.
40. Cortés R, Barragán ER, López VH, Ambriz RR, Jaramillo D. Mechanical properties of Inconel 718 welds performed by gas tungsten arc welding. Int J Adv Manuf Technol. 2018;94:3949–61. https://doi.org/10.1007/s00170-017-1128-x.
41. DuPont JN, Robino CV. Influence of Nb and C on the solidification microstructures of Fe-Ni-Cr alloys. Scr Mater. 1999;41:449–54. https://doi.org/10.1016/S1359-6462(99)00102-5.
42. Gabrel J, Bendick W, Vandenberghe B, Lefebvre B, Gabrel J, Bendick W, Vandenberghe B, Lefebvre B. Status of development

of VM 12 steel for tubular applications in advanced power plants. Energy Mater. 2016;1:218–22.
43. Fu JW, Yang YS, Guo JJ. Formation of a blocky ferrite in Fe-Cr-Ni alloy during directional solidification. J Cryst Growth. 2009;311:3661–6. https://doi.org/10.1016/j.jcrysgro.2009.05.007.
44. Cortés R, Rodríguez NK, Ambriz RR, López VH, Ruiz A, Jaramillo D. Fatigue and crack growth behavior of Inconel 718–AL6XN dissimilar welds. Mater Sci Eng A. 2019;745:20–30. https://doi.org/10.1016/j.msea.2018.12.087.
45. Kulkarni A, Dwivedi DK, Vasudevan M. Dissimilar metal welding of P91 steel-AISI 316L SS with Incoloy 800 and Inconel 600 interlayers by using activated TIG welding process and its effect on the microstructure and mechanical properties. J Mater Process Technol. 2019;274: 116280. https://doi.org/10.1016/j.jmatprotec.2019.116280.
46. Saini N, Mulik RS, Mohan M. Influence of filler metals and PWHT regime on the microstructure and mechanical property relationships of CSEF steels dissimilar welded joints. Int J Press Vessel Pip. 2019;170:1–9. https://doi.org/10.1016/j.ijpvp.2019.01.005.
47. Chai X, Bundy JC, Amata MA, Zhang C, Zhang F, Chen S, Babu SS, Kou S. Creep rupture performance of welds of P91 pipe steel. Weld J. 2015;94:145s.
48. Basturk SB, Dancer CEJ, McNally T. Role of dissimilar Ni-based ERNiCrMo-3 filler on the microstructure, mechanical properties and weld induced residual stresses of the ferritic/martensitic P91 steel welds joint. Int J Pressure Vessels Pip. 2020;1936:104743.
49. Saedi AH, Hajjari E, Sadrossadat SM. Microstructural characterization and mechanical properties of TIG-welded API 5L X60 HSLA steel and AISI 310S stainless steel dissimilar joints. Metall Mater Trans A Phys Metall Mater Sci. 2018;49:5497–508.
50. Dak G, Pandey C. Experimental investigation on microstructure, mechanical properties, and residual stresses of dissimilar welded joint of martensitic P92 and AISI 304L austenitic stainless steel. Int J Press Vessel Pip. 2021;194: 104536. https://doi.org/10.1016/j.ijpvp.2021.104536.
51. Kangazian J, Sayyar N, Shamanian M. Influence of microstructural features on the mechanical behavior of incoloy 825 welds. Metallogr Microstruct Anal. 2017;6:190–9. https://doi.org/10.1007/s13632-017-0353-x.
52. Aminipour N, Derakhshandeh-Haghighi R. The effect of weld metal composition on microstructural and mechanical properties of dissimilar welds between Monel 400 and Inconel 600. J Mater Eng Perform. 2019;28:6111–24. https://doi.org/10.1007/s11665-019-04328-0.
53. Dean D, Hidekazu M. Prediction of welding residual stress in multi-pass butt-welded modified 9Cr–1Mo steel pipe considering phase transformation effect. Comput Mater Sci. 2006;37:209–19. https://doi.org/10.1016/j.commatsci.2005.06.010.
54. Zhong W, Lin JL, Chen Y, Li Z, An K, Sutton BJ, Heuser BJ. Microstructure, hardness, and residual stress of the dissimilar metal weldments of SA508-309L/308L-304L. Metall Mater Trans A Phys Metall Mater Sci. 2021;52:1927–38.
55. Li S, Hu L, Dai P, Bi T, Deng D. Influence of the groove shape on welding residual stresses in P92 / SUS304 dissimilar metal butt-welded joints. J Manuf Process. 2021;66:376–86. https://doi.org/10.1016/j.jmapro.2021.04.030.
56. Zhao L, Liang J, Zhong Q, Yang C, Sun B, Du J. Numerical simulation on the effect of welding parameters on welding residual stresses in T92/S30432 dissimilar welded pipe. Adv Eng Softw. 2014;68:70–9. https://doi.org/10.1016/j.advengsoft.2013.12.004.

Authors and Affiliations

Gaurav Dak[1] · Chandan Pandey[1]

[1] Department of Mechanical Engineering, Indian Institute of Technology (IIT) Jodhpur, 342037, Karwar, Rajasthan, India